



HAL
open science

A mesoscopic model for the rheology of soft amorphous solids, with application to mi- crochannel flows

Alexandre Nicolas, Jean-Louis Barrat

► To cite this version:

Alexandre Nicolas, Jean-Louis Barrat. A mesoscopic model for the rheology of soft amorphous solids, with application to mi- crochannel flows. 2013. hal-00832374v2

HAL Id: hal-00832374

<https://hal.science/hal-00832374v2>

Preprint submitted on 9 Jul 2013

HAL is a multi-disciplinary open access archive for the deposit and dissemination of scientific research documents, whether they are published or not. The documents may come from teaching and research institutions in France or abroad, or from public or private research centers.

L'archive ouverte pluridisciplinaire **HAL**, est destinée au dépôt et à la diffusion de documents scientifiques de niveau recherche, publiés ou non, émanant des établissements d'enseignement et de recherche français ou étrangers, des laboratoires publics ou privés.

A mesoscopic model for the rheology of soft amorphous solids, with application to microchannel flows

Alexandre Nicolas,^a and Jean-Louis Barrat,^{*a‡}

Received Xth XXXXXXXXXXXX 20XX, Accepted Xth XXXXXXXXXXXX 20XX

First published on the web Xth XXXXXXXXXXXX 200X

DOI: 10.1039/c000000x

We study a mesoscopic model for the flow of amorphous solids. The model is based on the key features identified at the microscopic level, namely periods of elastic deformation interspersed with localised rearrangements of particles that induce long-range elastic deformation. These long-range deformations are derived following a continuum mechanics approach, in the presence of solid boundaries, and are included in full in the model. Indeed, they mediate spatial cooperativity in the flow, whereby a localised rearrangement may lead a distant region to yield. In particular, we simulate a channel flow and find manifestations of spatial cooperativity that are consistent with published experimental observations for concentrated emulsions in microchannels. Two categories of effects are distinguished. On the one hand, the coupling of regions subject to different shear rates, for instance, leads to finite shear rate fluctuations in the seemingly un-sheared “plug” in the centre of the channel. On the other hand, there is convincing experimental evidence of a specific rheology near rough walls. We discuss diverse possible physical origins for this effect, and we suggest that it may be associated with the bumps of particles into surface asperities as they slide along the wall.

Contents

1	Introduction	2
2	Continuum-mechanics based description of plastic events and presentation of the mesoscopic model	4
2.1	Description of a plastic event	4
2.2	Calculation of the elastic deformation induced by a single plastic event (2D, tensorial)	6
2.3	Implementation of parallel confining walls	8
2.4	Dynamics of the model and space discretisation	11
2.5	Coarse-grained convection	11
2.6	Probabilities for the onset and end of a plastic event	12

^a Laboratoire Interdisciplinaire de Physique, Université Joseph Fourier Grenoble, CNRS UMR 5588, BP 87, 38402 Saint-Martin d’Hères, France

3	Fitting of model parameters & General observations in a channel flow	13
3.1	Fitting of model parameters	13
3.2	Channel flow: general observations	14
4	Cooperativity in the bulk flow: a manifestation of the coupling between heterogeneous regions	17
4.1	Origin and description of the nonlocality in the flow	17
4.2	Nonlocal effects in the velocity profiles	18
4.3	Shear rate fluctuations in the plug	21
5	A specific rheology near the walls?	23
5.1	Weak deviations due to no slip boundary condition	23
5.2	Physical effect of rough walls	24
5.3	Fictitious plastic events along the wall as mechanical noise sources	26
6	Conclusions & Outlook	28
A	Derivation of the correction terms to the propagator for a system bounded by walls	32
B	Calculation of the line-averaged velocity	35
C	Estimation of the deviations due to bulk cooperativity	36

1 Introduction

The flow of simple fluids can be described microscopically as a succession of local, independent processes: collisions in the kinetic theory picture or hopping events in the classical Eyring description. As the temperature is lowered, or as the density increases, these processes tend to become more collective, with a dynamical length scale that increases as the glass transition is approached^{1,2}. Eventually, the liquid falls out of equilibrium and acquires a nonzero shear modulus on any finite time scale, as well as a yield stress that must be overcome in order to initiate the flow. Similar changes take place in athermal materials when the jamming point is crossed following an increase of density. It is now quite well established³ that the flow mechanisms of such amorphous solids are different in essence from those of liquids, as they involve elastic interactions (shear waves) that are transmitted through solids, but not through fluids. This results in nonlocal effects in the flow of soft jammed/glassy materials, contrasting the case of a simple fluid.

In fact, the flow of these materials bears notable similarities with the dynamics of earthquakes⁴, in that it features a solid-like behavior at rest and local yielding above a given applied stress. Yielding is characterized by the emergence of local 'shear transformations' involving a few particles⁵, associated with a local fluidisation of the material. These structural rearrangements, hereafter named plastic events, and also often referred to as shear transformations, or shear transformation zones, in the literature, induce long-range deformations. The microscopic details vary to some extent with the particular nature of the material. In the

case of foams, they are identified as T1 events, in which the local change of first neighbors is mediated by an unstable stage with four bubbles sharing one vertex. In colloidal pastes and in atomic systems, they involve relative displacements of limited magnitude within a small group of atoms, which lead to a new equilibrium configuration that is related to the original one by a shear deformation. In all cases the stress that was originally supported by the particles partaking in the plastic event is transmitted to the surrounding medium, which behaves as an elastic continuum. The robustness of the above scenario for an extremely wide range of materials is striking. Ample evidence of the local plastic events and their long-range effects is indeed provided both by experiments using diverse materials and simulations^{6–8}.

In the last two decades the modelling of flow in amorphous systems has evolved along two distinct, but related, lines. First, several models have been proposed that incorporate the flow scenario in an average description. These models, among which the shear transformation zone⁹ and the soft glassy rheology (SGR)^{10,11} models are the most sophisticated examples. Other simplified models falling into the same category are the fluidity model¹² or the very simple λ model¹³ describe the average evolution of a population of flow defects under an imposed strain rate in a mean-field-like manner. The effect of elastic interactions between these defects is not directly accounted for, but enters the models indirectly *via* the introduction of parameters such as an effective temperature associated with the mechanical noise. These approaches have been remarkably successful in describing at least some aspects of steady state flow curves, e.g., the existence of a yield stress and the low shear rate behaviour, as well as transient or oscillatory response in various systems, from metallic glasses to foams or colloidal pastes. However, due to their intrinsic mean field nature, fluctuations and spatial correlations in the flow are discarded. Also, in their most simplified version they are unable to account for heterogeneities and strain localisation. To capture the latter phenomenon, extensions of the models have introduced a coupling between the mean-field description and a diffusive behaviour of the effective temperature, which again can be understood as a consequence of the non-local interaction between elementary flow events^{14–16}.

An alternative line of modelling consists in implementing numerically the scenario of plastic events interacting through an elastic continuum in the form of a discrete lattice model. Such an approach was pioneered by Chen, Bak and Obukhov, in a model initially proposed for the description of earthquakes¹⁷, and by Argon and Bulatov^{18–20}. A number of similar *mesoscopic* models based on the same physical scenario, but with different implementations, have been proposed and studied in the literature^{21–23}. The models are able to produce flow curves sharing similarities with those observed experimentally, although significant differences are revealed by closer inspection; they can account for strain localisation and its dependence on the local dynamical rules^{23,24}, and allow one to explore the influence of parameters such as ageing or temperature. They also reproduce the dynamical heterogeneities observed in the flow, and their variation with strain rate²⁵. However, these comparisons have generally remained qualitative, since the models are in general rather schematic, ignoring in particular tensorial aspects or convection.

In this contribution, we present a detailed study of a mesoscopic model that

incorporates these elements in a manner that allows a comparison with experimental data obtained in simple geometries. In particular, we will focus on the channel flow geometry and show that the model captures experimental observations, including the fluctuations in the local shear rates arising even in seemingly quiescent regions. Such fluctuations are the hallmark of non-locality and spatial cooperativity in the flow, which can give rise to spectacular long-range fluidisation phenomena.

Section 2 introduces the continuum mechanics-based description of a plastic event and presents our mesoscopic model. Details of its numerical implementation are also provided. In Section 3, we fit the parameters of the model to experimental data for concentrated emulsions taken from the literature, and we present the general features observed in our numerical simulations of a channel flow. The last two sections focus on the manifestations of spatial cooperativity in this particular geometry: Section 4 tackles cooperativity in the bulk, whereas some aspects of the specific rheology near a wall are addressed in Section 5. A shorter account of some of these results has been described in Ref.²⁶.

2 Continuum-mechanics based description of plastic events and presentation of the mesoscopic model

Under homogeneous driving conditions, simple fluids flow homogeneously. Amorphous solids, on the other hand, exhibit localised plastic events when they are forced to flow^{5,6,27–29}, associated with local shear transformations. In this section, we use an approach rooted in continuum mechanics to describe the effect of a plastic event on the surrounding (elastic) medium, along with its time evolution. Then, we show how these results are integrated into a mesoscopic model. The presentation of the model is brought to completion by the choice of relevant probabilities for the onset and end of a plastic event. This section extends and details previous presentations in Ref.^{22,26}.

2.1 Description of a plastic event

Consider a rectangular system described by Cartesian coordinates (x, y) , where $x \in [0, L_x]$ and $y \in [0, L_y]$ are the streamwise and crosswise coordinates, respectively. Should the system be unbounded, the following results will be applicable, provided that one takes their $L_x \rightarrow \infty$ and $L_y \rightarrow \infty$ limits. Otherwise, periodic boundary conditions are assumed, for the time being.

On account of the solidity of the material (which is preserved at low shear rate), the response of the system to a perturbation can be modelled by Hooke's law, whereby the local elastic stress σ^{el} is related to the local (deviatoric) strain ε via $\sigma^{el} = \mathbf{C}\varepsilon$, where \mathbf{C} is the stiffness matrix. Before a perturbation (here, a plastic event) sets in, mechanical equilibrium requires that:

$$\nabla \cdot (\mathbf{C}\varepsilon^{(0)}) - \nabla p^{(0)} = 0, \quad (1)$$

where p is the pressure, and the (0) superscripts denote the initial state. In the following, the material will be considered incompressible, which implies that the

displacement field u obeys $\nabla \cdot u = 0$, and isotropic, so that the elastic stress can be written, in condensed notations, as

$$\sigma^{el} = \mu \begin{pmatrix} \epsilon_{xx} - \epsilon_{yy} \\ \epsilon_{yy} - \epsilon_{xx} \\ 2\epsilon_{xy} \end{pmatrix} = 2\mu \begin{pmatrix} \epsilon_{xx} \\ -\epsilon_{xx} \\ \epsilon_{xy} \end{pmatrix} \equiv 2\mu\epsilon, \quad (2)$$

where μ is the shear modulus.

Clearly, Hooke's law will only hold within a certain limit. Indeed, when the configuration is too strained locally, say, in a region $\mathcal{S}^{(0)}$, particles rearrange so that the system is brought to a new local minimum: this is a plastic event. While this rearrangement occurs, the memory of the reference elastic configuration is lost, and, consequently, the local elastic stress vanishes. The region undergoing the rearrangement is therefore liquid-like and its stress will be mainly of dissipative origin. Following this line of thinking and neglecting inertia, the force equilibrium during the plastic rearrangement reads

$$\begin{cases} \nabla \cdot \sigma^{diss} - \nabla p = 0 & \text{in region } \mathcal{S}, \\ 2\mu\nabla \cdot \epsilon - \nabla p = 0 & \text{outside region } \mathcal{S}. \end{cases} \quad (3)$$

Notice that the boundaries of the plastic region shall be deformed during the event and \mathcal{S} refers to the *deformed* region. In Eqs.3, the dissipative stress σ^{diss} was supposed to be mainly concentrated in the rearranging region. For simplicity, we further assume that dissipation is linear with respect to the strain rate, viz. $\sigma^{diss} = 2\eta_{eff}\dot{\epsilon}$. This linearity is naturally to be understood as a simplification, and not as a claim of the existence of some universality regarding the dissipative mechanism (see Ref.³⁰ for a non-linear law in the case of a foam). In addition to Eqs.3, force balance requires the continuity of the stress all along the boundary of region \mathcal{S} . If \mathcal{S} is small enough so that the (plastic) deformation rate in this region can be considered homogeneous, viz., $\dot{\epsilon}(r) \equiv \dot{\epsilon}^{pl}$ for $r \in \mathcal{S}$, the continuity of the stress all along the boundary $\partial\mathcal{S}$ of the plastic inclusion leads to:

$$\dot{\epsilon}^{pl} = \frac{1}{\tau} \epsilon_{\partial\mathcal{S}}, \quad (4)$$

where $\epsilon_{\partial\mathcal{S}}$ refers to the (elastic) strain on the outer boundary $\partial\mathcal{S}$. The time scale $\tau \equiv \frac{\eta_{eff}}{\mu}$ for the viscous dissipation of the elastic energy has been made apparent.

The *leading-order* response of the system to the plastic event immediately follows from Eq. 4: it simply comes down to a (plastic) strain rate $\dot{\epsilon}^{pl}(t) = \frac{1}{\tau} \epsilon_{\partial\mathcal{S}}^{(0)}$ affecting only region \mathcal{S} . In an unconstrained environment, the inclusion would therefore undergo a deformation $\dot{\epsilon}^{pl} dt$ in a time interval dt .

However, since the inclusion is embedded in a solid, the latter reacts to this plastic strain: supplementary elastic stress and pressure fields, $\sigma^{(1)} dt = 2\mu\dot{\epsilon}^{(1)} dt$ and $\dot{p}^{(1)} dt$ respectively, are thereby induced in the medium*. The derivation of the fields $\sigma^{(1)}$ and $\dot{p}^{(1)}$ is presented in the next subsection. For the time being, let us remark that, thanks to the linearity of the equations, one can express the induced stress on the boundary $\partial\mathcal{S}$ as

$$\sigma_{\partial\mathcal{S}}^{(1)} = 2\mu\mathcal{G}_0\dot{\epsilon}^{pl}, \quad (5)$$

* This deformation will, in turn, affect the plastic deformation rate $\dot{\epsilon}^{pl}$, but these higher order effects are neglected here.

where \mathcal{G}_0 is a yet unknown tensor. Now, since the response of the solid is a *reaction* to an imposed shear strain $\dot{\epsilon}^{pl} dt$, it will *oppose* it, at least in the direct vicinity of the inclusion. Therefore, one expects the eigenvalues of \mathcal{G}_0 to be *negative*. Inserting Eqs. 2 and 4 into Eq. 5 yields, after simplification:

$$\dot{\epsilon}_{\partial\mathcal{S}}^{(1)}(t) = \frac{\mathcal{G}_0}{\tau} \epsilon_{\partial\mathcal{S}}(t) \quad (6)$$

Equation 6 expresses the fact that, up to a (potentially time-dependent) shape prefactor \mathcal{G}_0 , the force driving the rearrangement is the elastic stress imposed on \mathcal{S} by the rest of the system, and that, in opposing this force, dissipation sets a *finite* timescale τ to this plastic transformation[†]. Cloitre and co-workers³² suggested that the duration of a rearrangement in soft colloidal pastes coincides with the shortest structural relaxation time τ_β , which also results from a “competition between elastic restoring forces and interparticle friction”, and experimentally confirmed the proposed scaling $\frac{\eta_{eff}}{\mu}$ for the latter time (where η_{eff} is determined by the dissipation within lubrication films). This scaling was also used to collapse flow curves onto a single master curve, which bolsters its relevance for the rheology of these materials.

2.2 Calculation of the elastic deformation induced by a single plastic event (2D, tensorial)

Reference³³ proposed a method to derive the fields $\dot{\epsilon}^{(1)} dt$ and $\dot{p}^{(1)} dt$ induced by the plastic strain $\dot{\epsilon}^{pl} dt$, in a simplified context. First, one considers the limit of an infinitely small plastic inclusion \mathcal{S} , $\epsilon^{pl}(r) \rightarrow \epsilon^{pl} a^2 \delta(r - r_0)$, where r_0 is the centre of region \mathcal{S} , and a , the typical linear size of \mathcal{S} . (The dots indicating derivation w.r.t. time are omitted in this section). Secondly, by virtue of the linearity of the equations, the inclusion applies a stress $\sigma^{inc} = 2\mu\alpha\epsilon^{pl}$ on its surrounding, where α is a scalar (instead of a tensor) because of symmetry arguments. At the expense of a renormalisation of the timescale τ appearing in the definition of $\dot{\epsilon}^{pl}$, Eq. 4, *viz.* $\tau \equiv \alpha^{-1} \frac{\eta_{eff}}{\mu}$, we can consider that $\alpha = 1$. Mechanical equilibrium in the solid then reads:

$$2\mu\nabla \cdot [\epsilon^{(1)}] - \nabla p^{(1)} = 2\mu\nabla \cdot [\epsilon^{pl} a^2 \delta(r - r_0)] \quad (7)$$

To pursue, Eq. 7 is solved with the help of the Oseen-Burgers tensor O , expressed in Fourier coordinates $\underline{q} \equiv (p_m, q_n)$, where $p_m \equiv \frac{2\pi m}{L}$ and $q_n \equiv \frac{2\pi n}{L}$, with $m, n \in \mathbb{Z}$:

$$\hat{O}(\underline{q}) = \frac{1}{\mu q^2} \left(1 - \frac{1}{q^2} \underline{q} \otimes \underline{q} \right). \quad (8)$$

The Oseen-Burgers tensor is the elementary solution in terms of displacement u of the equations $\{2\mu\nabla \cdot \epsilon - \nabla p = \delta(r), \text{div}(u) = 0\}$, where the linearised deformation tensor obeys $\epsilon = \frac{\nabla u + (\nabla u)^T}{2}$, with the boundary conditions specified above.

[†] The *finite* duration of a plastic rearrangement, which is neglected in the Soft Glassy Rheology model¹⁰, the Kinetic Elastoplastic model¹⁶, as well as in the mesoscopic models of Refs. ^{21,23}, might play a crucial role in the compressed exponential relaxation of different soft materials. For details, see Ref. ³¹.

Therefore,

$$u^{(1)}(\underline{q}) = 2\mu \hat{O}(\underline{q}) \cdot (-i\underline{q} \cdot \hat{\epsilon}^{pl}). \quad (9)$$

Recalling Hooke's law, $\hat{\sigma}^{(1)}(\underline{q}) = 2\mu \left[i \frac{q \otimes u^{(1)} + (q \otimes u^{(1)})^T}{2} - \hat{\epsilon}^{pl}(\underline{q}) \right]$, one finally arrives at:

$$\begin{pmatrix} \hat{\epsilon}_{xx}^{(1)} \\ \hat{\epsilon}_{xy}^{(1)} \end{pmatrix}(\underline{q}) = \hat{G}^\infty(\underline{q}) \cdot \begin{pmatrix} \hat{\epsilon}_{xx}^{pl} \\ \hat{\epsilon}_{xy}^{pl} \end{pmatrix}(\underline{q}) \quad (10)$$

where the elastic propagator \hat{G}^∞ obeys:

$$\hat{G}^\infty(\underline{q}) \equiv \frac{1}{q^4} \begin{bmatrix} -(p_m^2 - q_n^2)^2 & -2p_m q_n (p_m^2 - q_n^2) \\ -2p_m q_n (p_m^2 - q_n^2) & -4p_m^2 q_n^2 \end{bmatrix}. \quad (11)$$

Equations 10 and 11 express the elastic deformation field induced by a pointlike plastic event in a system with periodic boundary conditions. The corresponding stress field is straightforwardly obtained by multiplication with the shear modulus 2μ .

In real space, the propagator expressed in Eq. 11 has a four-fold angular symmetry and decays as r^{-d} , where $d = 2$ is the spatial dimension. These properties are consistent with observations from atomistic simulations^{6,28,34} as well as experiments³⁵.

Note that the present treatment does not describe the dilational effects³⁶ possibly taking place during plastic events. These effects may naturally add quantitative corrections to the picture drawn here, but, along with the associated flow concentration coupling³⁷ and free volume diffusion mechanisms (see Ref.¹⁴ and references therein), they are probably not of paramount importance in the high density-low temperature situations considered here³⁸, where such effects are not always present^{39,40}.

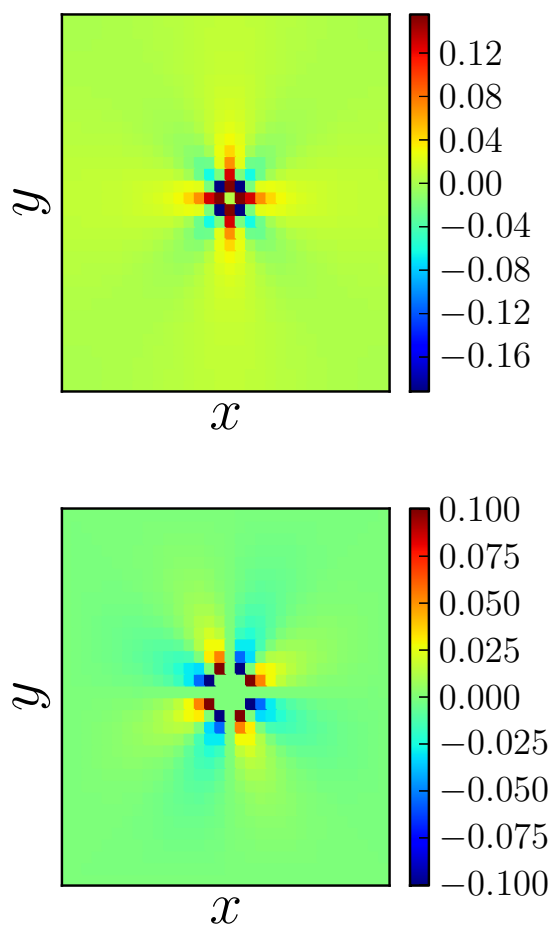


Fig. 1 Deformation field $\epsilon^{(1)}$ induced by a single plastic event ϵ_{xy}^{pl} . Top: $\epsilon_{xy}^{(1)}$ component; bottom: $\epsilon_{xx}^{(1)}$ component. The values are normalised by the absolute value of the locally induced deformation $\epsilon_{xy}^{(1)}$. Because of the comparatively large (in magnitude) peak value at the origin, the central block has been artificially coloured.

2.3 Implementation of parallel confining walls

In order to study a genuine channel geometry, the boundary conditions need to be adapted to take into account two infinite parallel walls, directed along e_x , bounding the flow, while keeping the periodicity in direction e_x . The effect of the walls is modelled by imposing a no-slip boundary conditions at their locations, in line with what is commonly done in fluid mechanics.

To implement the no-slip boundary conditions, we extend the treatment of Ref.³³: the system is duplicated in the direction perpendicular to the walls, so that the region $y \in [0, L_y]$ describes the real system, while the region $y \in [-L_y, 0]$ is fictitious. For each plastic event (in the real system), a symmetric 'image plastic

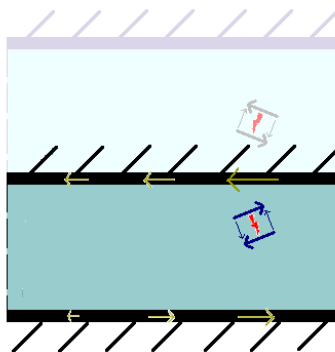


Fig. 2 Sketch of the duplicated system.

event' is created in the fictitious half. The y -component of the velocity field is thereby cancelled at the walls. To remove the x -component of the velocity, adequate forces directed along e_x are added along the walls. These (fictitious) forces add a corrective term $\hat{\varepsilon}^{corr}$ to the deformation field $\hat{\varepsilon}^\infty$ obtained for periodic boundary:

$$\hat{\varepsilon}(\underline{q}) = \hat{\varepsilon}^\infty(\underline{q}) + \hat{\varepsilon}^{corr}(\underline{q}).$$

The calculation of $\hat{\varepsilon}^{corr}(\underline{q})$ presented in Appendix A yields the following result:

$$\begin{pmatrix} \hat{\varepsilon}_{xx}^{corr}(p_m, q_n) \\ \hat{\varepsilon}_{xy}^{corr}(p_m, q_n) \end{pmatrix} = \begin{pmatrix} \frac{-2p_m q_n^2}{q^4} \left[i \sum_y \zeta_\delta(X) \mathcal{F}_x \varepsilon_{xy}^{pl}(p_m, y) + 2 \sum_y \xi_\delta(X) \mathcal{F}_x \varepsilon_{xx}^{pl}(p_m, y) \right] \\ \frac{q_n(p_m^2 - q_n^2)}{q^4} \left[i \sum_y \zeta_\delta(X) \mathcal{F}_x \varepsilon_{xy}^{pl}(p_m, y) + 2 \sum_y \xi_\delta(X) \mathcal{F}_x \varepsilon_{xx}^{pl}(p_m, y) \right] \end{pmatrix}, \quad (12)$$

where \sum_y denotes an integral over all streamlines $y = cst$ and \mathcal{F}_x indicates a Fourier transformation along direction x . X is used as a shorthand for $\left(\frac{\pi y_{ev}}{L_y}, \frac{p_m L_y}{\pi}\right)$ and the analytical expressions of the functions $\zeta_\delta(X)$ and $\xi_\delta(X)$ can be found in Appendix A.

Note that the corrective term couples the different Fourier modes so that the translation invariance of the propagator \mathcal{G} is broken (in the y -direction). In particular, for a given plastic strain, the local strain response now depends upon the distance to the wall. The dependence on the distance for a plastic event $\left\{ \varepsilon_{xx}^{pl} = 0, \varepsilon_{xy}^{pl} \neq 0 \right\}$ is presented in Fig.3 for a system that is coarse-grained into blocks of unit size (see next section). In particular, one can see that the local strain relaxation induced by a given plastic strain is around 35% higher in the direct vicinity of a wall than in the bulk case, owing to the vicinity of a solid boundary.

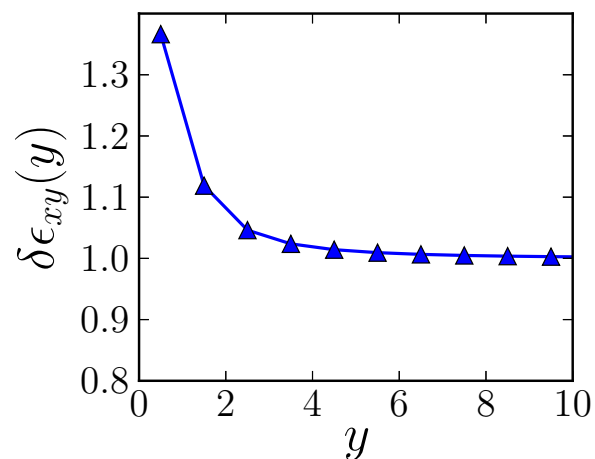


Fig. 3 Decrease $|\epsilon_{xy}^{(1)}|$ of the *local* elastic strain induced by a given plastic strain ϵ_{xy}^{pl} as a function of the distance y to the wall (expressed in block units, which is the only relevant length scale). Values have been normalised to the 'bulk' value, that is, the quantity measured infinitely far from the wall.

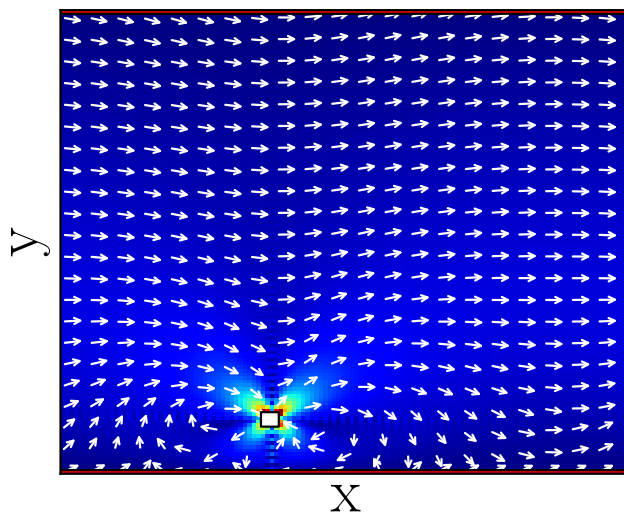


Fig. 4 (Colour online) Displacement field induced by a single plastic event (located in the white square). The white arrows show the direction of the field, while the colour code represents the displacement amplitude (brighter colours indicate higher amplitude). Walls, drawn as red lines, are present at the top and at the bottom of the system.

2.4 Dynamics of the model and space discretisation

At every point in space, the dynamics is governed by the following equation, including both the external driving $\dot{\Sigma}^{ext}$ and the (local and nonlocal) stress redistribution due to plastic events:

$$\partial_t \sigma(r) = \dot{\Sigma}^{ext}(r) + \int \mathcal{G}(r, r') \cdot 2\mu \dot{\epsilon}^{pl}(r') d^2 r', \quad (13)$$

where $\dot{\epsilon}^{pl}(r) = \frac{\dot{\sigma}(r)}{2\mu\tau}$ if r is in a plastic region, $\dot{\epsilon}^{pl}(r) = 0$ otherwise, and the propagator \mathcal{G} takes into account both the bulk (periodic) contribution and the corrections due to the presence of walls. The plastic activity is determined by checking at every time step, and at every point in space, the elements that undergo a plastic event. The criterion for triggering plastic events will be discussed in the next section. The time derivative in Eq. 13 is handled numerically with a Eulerian procedure, with time step $dt \leq 0.01\tau$.

The convolution part of Eq. 13 is most easily solved in Fourier space, where the convolution turns into a product involving the propagator derived previously (see Eqs. 11 and 13, for the two contributions to \mathcal{G}). To prepare the use a Fast Fourier Transform routine, the system is spatially coarse-grained into a rectangular lattice of square-shaped blocks of unit size. Physically, the size of the blocks should correspond to the spatial extent of a plastic event.

Technically, the slow decay of $\hat{\sigma}_{xx}(q)$ with q generates some irregularities in the computation of the associated back-Fourier transform. Accordingly, for the sake of precision, we use a finer mesh for the computation of the Fourier transformations, i.e., we divide each block into four subblocks, so that each plastic event now spans four subblocks. Thanks to this technical trick, a smooth stress field is recovered, as shown in Fig. 1.

Besides, mechanical equilibrium requires that the average of the shear stress over any streamline (or any line with a given direction) be homogeneous. However, the assumption of pointwise plastic events combined with the discretisation of space is not entirely consistent, insofar as it results in moderate violations of the aforementioned homogeneity, when plastic events are far off the direction of macroscopic shear. In order to restore homogeneity, an *ad-hoc* shear stress is added globally to every streamline. We have checked that this procedure has very little effect on the results presented below.

2.5 Coarse-grained convection

Although the presence of a lattice precludes a rigorous implementation of convection, a coarse-grained version can be introduced as follows: The average velocity of each streamline in the flow direction is rigorously calculated at each time step., viz.

$$\begin{aligned} \langle u_x \rangle_x(y_0) &\equiv \frac{1}{L_x} \int_{-L_x/2}^{L_x/2} u_x(x, y_0) dx \\ &= \sum_{y_{ev}} \left[\text{sign}(y_0 - y_{ev}) \cdot \left(1 - \frac{|y_0 - y_{ev}|}{L_y} \right) + 1 - \frac{y_{ev}}{L_y} - \frac{y_0}{L_y} \right] \mathcal{F}_x \epsilon_{xy}^{pl}(m=0, y_{ev}). \end{aligned}$$

Details of the algebra are provided in Appendix B. The line displacement can thus be updated at each time step. Whenever the displacement on a line grows larger than a multiple of the unit block size, this line is incrementally shifted of the adequate number of units, as a whole. In so doing, the regularity of the lattice is preserved.

A technical detail might be worth mentioning: A naïve implementation of the above method results in a violation of Galilean invariance, insofar as lines with lower *velocity* will be shifted less often than others (artificial pinning) and therefore will tend to conserve their neighbours (in the velocity gradient direction) for a longer time - whereas the motion with respect to neighbouring lines should be exclusively controlled by the local shear rate. It turns out that, in a simple shear situation, the system is quite sensitive to such a bias, which may lead 'pinned' lines to concentrate more plastic activity. The practical solution to this issue consists in adding a random offset displacement to *all* streamlines, so that no artificial pinning can occur.

2.6 Probabilities for the onset and end of a plastic event

So far, we have quantitatively described the effect of a plastic event and detailed its derivation from rather well established principles. In order to complete the model, criteria must now be fixed with regard to the onset and termination of a plastic event. Since the mesoscopic model is oblivious to the microscopic arrangement of the particles and their stability, the criteria will obviously be somewhat arbitrary. In the present model, they will involve two rates, $l(\sigma)$ and $e(\sigma)$, which govern, respectively, the transition from the elastic to the plastic regime and the recovery of elastic behavior after initiation of the plastic event,

$$\text{elastic regime} \xrightleftharpoons[e(\sigma)]{l(\sigma)} \text{plastic event.}$$

The use of rates introduces a simple element of stochasticity in the model, and indirectly accounts for the variability of local environments.

Let us consider a mesoscopic region susceptible of undergoing a plastic rearrangement. In the elastic regime, its configuration minimises the potential energy, under the stress/strain constraints imposed at the boundaries by the rest of the material. The minimum is stable as long as $E - E_{\text{constraint}} \leq E_a$, where we assume the existence of an average energy barrier E_a . In an Eyring-like type of approach, the constraint is expressed as: $E_{\text{constraint}} \propto \sigma$, where σ is the local stress applied by the outer region, and we take an activation volume equal to unity. Consequently, the rate of plastic activation depends exponentially on the local stress. In the following, we will use the expression

$$l(\sigma) = \Theta(\sigma - \sigma_{\text{ly}}) \exp\left(\frac{\sigma - \sigma_{\text{y}}}{x_{\text{loc}}}\right) \tau^{-1}$$

Three parameters have been introduced in this expression: σ_{y} is the yield stress associated to the average energy barrier; x_{loc} is a material-dependent activation temperature. Unlike the effective temperatures used in the Soft Glassy Rheology model¹¹ or the stress fluctuation approach à la Eyring⁴¹, x_{loc} only accounts for local microscopic effects and does *not* include the local stress fluctuations due to

stress redistribution, i.e., mechanical noise: the latter should emerge naturally as a consequence of long range interactions between events, within the framework described above. Note that the limit $x_{loc} \rightarrow 0$ of the activation rate coincides with the usual von Mises yielding criterion, which states that the material yields if and only if $\sigma \geq \sigma_y$. However, under shear stress, the effective lowering of energy barriers results in the necessity to preserve the possibility of activated events, even in materials usually referred to as athermal at rest. For instance, the occurrence of rearrangements in granular matter long after shear cessation⁴² supports this claim, although the physical reason for such rearrangements is far from clear. Another possible justification for introducing x_{loc} may be that it effectively accounts for some dynamical disorder in the local yield stress. Finally, we found that introducing this fluctuating, apparently activated character in the yield criterion is the only way to obtain flow curves in reasonable agreement with experimental data, as shown below.

The parameter $\sigma_{\mu y}$ in the Heaviside function Θ is a critical stress, intended to be small $\sigma_{\mu y} \ll \sigma_y$ and below which no rearrangement can occur. Clearly, this is an *ad hoc* approach to conserve a finite macroscopic yield stress in the limit of vanishing shear rate $\dot{\gamma}_{app} \rightarrow 0$, when no ageing process is explicitly taken into account. Note that Amon *et al.*⁴³, in a paper investigating the behaviour of granular matter on a tilted plane, recently called for a model displaying two critical stresses, with a microfailure stress in addition to the macroscopic one, although with a distinct definition.

A plastic event lasts until the local configuration gets trapped in a new potential well. This trapping is expected to occur when the local energy reaches low enough values, or, equivalently (recall that $\sigma^{diss} \propto 2\mu\epsilon_{\partial S}$, see Eq. 4), when the dissipative stress is dominated by the local elastic stress (which was neglected in Eq. 4). Consequently, we define an associated threshold for the recovery of elastic stability, whose value is set to $\sigma_{\mu y}$ in order to limit the number of parameters. Introducing a new intensive parameter x_{res} , this allows us to write the rate at which elastic behaviour is recovered as: $e(\sigma) = \exp\left(\frac{\sigma_{\mu y} - \sigma}{x_{res}}\right) \tau^{-1}$.

The definition of the rates e and l completes the description of the model. At each time step, the probability of failure of an elastic element is $l(\sigma)dt$, while the probability that a plastic element becomes elastic again is $e(\sigma)dt$.

3 Fitting of model parameters & General observations in a channel flow

In order to test the validity of the mesoscopic model presented in the previous section, we start by fitting the model parameters by comparing the flow curve obtained in simulations of a simple shear setup to experimental results for a concentrated emulsion.

3.1 Fitting of model parameters

We use units of time and stress such that $\tau = 1$ and $\sigma_y = 1$, and we set $\mu/\sigma_y = 1$ (note that the value of $\mu/\sigma_y = 1$ only contributes to rescaling the shear rate if convection is omitted). The model then involves three parameters, $\sigma_{\mu y}$, x_{loc} and

x_{res} .

In the following, our numerical simulations are compared to experimental data for concentrated oil-in-water emulsions collected by two different groups, Goyon et al.⁴⁴ and Jop et al.⁴⁵. The experimental systems are concentrated emulsions of $6 - 7\mu\text{m}$ droplets of silicon oil in a water-glycerol mixture at an oil volume fraction $\phi \sim 0.75$ significantly larger than the jamming volume fraction. Both groups report a Herschel-Bulkley dependence of the shear stress on the shear rate, that is, $\sigma = \sigma_d \left[1 + (\tau_{HB}\dot{\gamma})_{app}^n \right]$, with an exponent $n \simeq 0.5$ in both cases.

This Herschel-Bulkley law allows us to fit the remaining model parameters. To do so, we simulate a simple shear flow by setting the driving force to $\dot{\Sigma}_{app} = \mu\dot{\gamma}_{app}$ in Eq.13, with a stressless state as initial condition. By varying the parameters, we find that the combination $\{\sigma_{\mu y} = 0.17, x_l = 0.249, x_e = 1.66\}$ provides a quite satisfactory fitting of the flow curve, as shown in Fig.5. Note that model units of time and stress have been appropriately rescaled in the figure, to allow for comparison with the experimental values. Of course, one may argue that the fitting to the flow curve only loosely constrains the parameters, implying that other combinations of parameters could yield the same result. Nevertheless, we would like to mention that, when starting with a moderately different set of parameters and fine-tuning it to better match the data, we have recovered parameters similar to those selected.

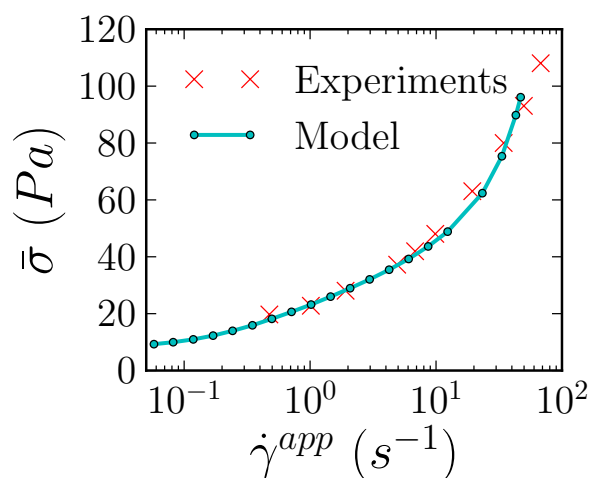


Fig. 5 (Crosses) Experimental and (dots) simulated flow curve. The experimental were obtained by Goyon et al. for an emulsion of $\sim 6.5\mu\text{m}$ silicon oil droplets in a water-glycerin mixture at volume fraction $\phi = 75\%$. The solid line is a guide to the eye.

3.2 Channel flow: general observations

Having set the model, we now turn to the specific case of channel flow. Indeed, many intriguing experimental results have been reported concerning the flow of soft jammed/glassy materials in that geometry^{39,44-48}, which is also relevant for practical applications, in particular in the area of microfluidics.

First of all, it is important to realise that, unlike the simple shear case, the flow is pressure driven in a channel flow, instead of being strain driven. Recalling that the driving Σ^{ext} in Eq.13 corresponds to the response of a purely elastic solid, it immediately follows that: $\dot{\Sigma}^{ext} = 0$, $\sigma_{xy}(x, y, t = 0) = \nabla p (y - L_y/2)$. Note the streamline-averaged stress conserves a linear profile throughout the simulation, because plastic events induce a homogeneous streamline-averaged stress, owing to mechanical equilibrium.

We first discuss some general features of the flow of soft jammed solids in that geometry. Conspicuous is, in the first place, the presence of a "plug" in the centre of the channel, i.e., a solid-like region in which the material is convected, but not sheared. The plug can clearly be seen in Fig.6, which demonstrates a nice agreement between the numerical and the experimental (time averaged) velocity profiles across the channel. Note that showing the velocity differences with respect to the maximal velocity across the channel obviates the experimental issue of the determination of wall slip.

However, averaging over time masks the temporal fluctuations of the flow. If one heeds the variations of the maximal streamline velocity of the simulated flow with respect to time, flow intermittency becomes evident [‡]. This phenomenon is more acute for narrow channels (see Fig.8), in agreement with results from numerical simulations regarding the effect of confinement (see Ref. ⁴⁰ and references therein). Note that flow intermittency, or "stick-slip" behaviour, has often been reported experimentally, but it has been interpreted in various ways depending on the particular system under study: the creation and failure of force chains is put forward in the case of granular matter ^{49,50}, while variations in the local concentrations of colloids and erosion by the solvent have been reported for concentrated colloidal suspensions ⁴⁸.

The spatial distribution of plastic events is also of interest. Indeed, although the plug remains virtually still on average, sparse plastic events are clearly seen to occur in that region, especially for narrow channels, and, consequently, below the bulk yield stress. Therefore, these plastic events essentially originate in cooperative effects, via the redistribution of stress generated by distant plastic events. Being of cooperative nature, the principal direction of their stresses at the yielding point (the 'angle of yield' of the plastic event) is broadly dispersed, since it is not strongly biased by a fixed applied shear (see Fig.7).

[‡] However, these fluctuations would presumably vanish in our model if the channel were of infinite length.

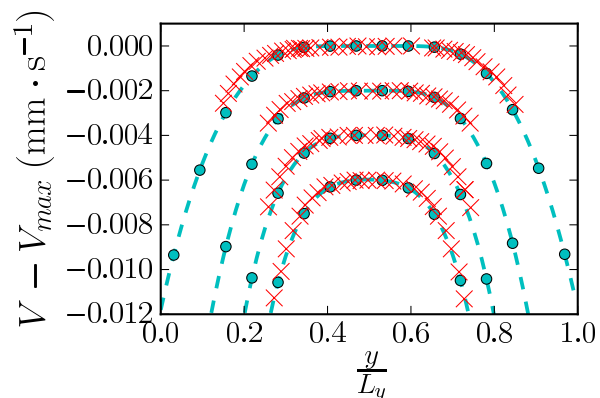


Fig. 6 (Crosses) Experimental and (dots) simulated velocity profiles, for stresses at the wall $\sigma_w = 141$ Pa, 188 Pa, 235 Pa, 282 Pa, corresponding to $\sigma_w = 0.36, 0.48, 0.60, 0.72$ in model units, from top to bottom. The experimental data are a courtesy of Jop *et al.*⁴⁵. The model time and stress units have been rescaled to match the experimental data.

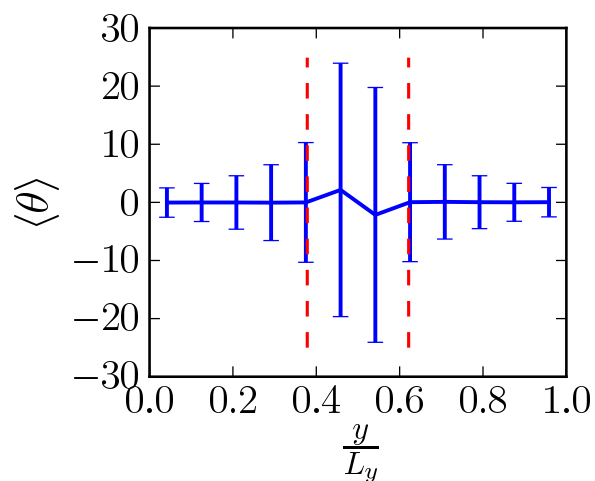


Fig. 7 Principal direction $\theta \in [-45^\circ, 45^\circ]$ of plastic events as a function of the position in the channel. Channel width: 12. $\sigma_w = 0.6$ in model units. The vertical dashed lines delimit the 'plug', i.e., the region where $|\langle \sigma_{xy} \rangle| \leq \sigma_d$. The bars give the standard deviation, $\pm \langle (\theta^2) - \langle \theta \rangle^2 \rangle$

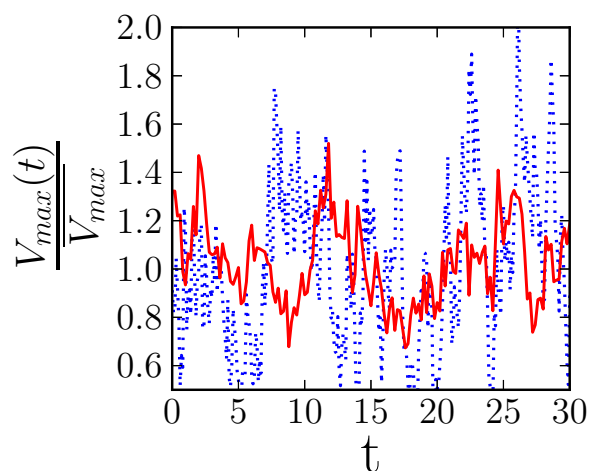


Fig. 8 Time variations of the maximal velocity in the channel, rescaled by its average value over time, for two channel widths: (solid red line) 24 blocks, (dotted blue line) 6 blocks.

4 Cooperativity in the bulk flow: a manifestation of the coupling between heterogeneous regions

4.1 Origin and description of the nonlocality in the flow

Spatial cooperativity is a hallmark of the flow of amorphous solids: Because of the solidity of these materials, shear waves can propagate in the bulk. Accordingly, a plastic event induces a long-range deformation of the material and can thus set off other plastic events, possibly triggering an avalanche. However, the channel geometry is particular in that the driving is intrinsically inhomogeneous; therefore, cooperativity couples regions (streamlines) subject to different stresses.

When considering a given region, one may then expect its behaviour to differ from that it would have in a homogeneous flow. This is a serious issue, since it undermines the paradigm that there exists a constitutive equation relating the local shear rate to the local shear stress, as explained by Goyon and colleagues^{39,44}. (Note, however, that doubts regarding the existence of a single flow curve for concentrated emulsions had also been voiced earlier, following experiments in a different geometry⁵¹).

To rationalise the deviations that they observed experimentally, Goyon et al.³⁹ made use of a diffusion equation operating on the local fluidity, that is to say, the inverse viscosity $f(r) \equiv \dot{\gamma}(r)/\sigma_{xy}(r)$:

$$\xi^2 \Delta f - (f - f_{\text{bulk}}[\sigma(y)]) = 0, \quad (14)$$

where $f_{\text{bulk}}(\sigma)$ denotes the fluidity measured in a homogeneous flow at applied stress σ . The length scale ξ is a cooperative length, that scales with the particle diameter^{39,52}. This diffusion equation is based on the idea that plastically active regions will fluidise their neighbours, and inversely. In Ref.¹⁶, Bocquet and

co-workers showed that this equation can formally be derived from a Hebraud-Lequeux fluidity model¹², provided heterogeneities are taken into account. However, the limitations imposed by analytical treatment required to cut off the propagator beyond the first neighbours, and to consider the limit of vanishing shear rate.

Nevertheless, Eq. 14 was found to provide a very satisfactory description of experimental and numerical data in several cases^{39,40,44–46,52}, provided that the parameters, that is, the cooperativity length ξ and the value f_{wall} of the fluidity at the wall, are carefully fitted.

Assuming that this equation offers a valid first-order approximation of the flow, we use it to assess the amplitude of the expected deviations from bulk behaviour.

To do so, we quantify the extent of the coupling by estimating the *relative* deviations $\delta f(y) \equiv f(y) - f_{\text{bulk}}$ of the fluidity. This defines a dimensionless number, the Babel number $\text{Ba} \equiv \frac{\delta f}{f}$. In Appendix C, we show that, under the assumption of a Herschel-Bulkley constitutive equation, Ba is of order $\left(\xi \frac{\|\nabla\sigma\|}{\sigma - \sigma_d}\right)^2$, that is, $\left(\xi \frac{\|\nabla p\|}{\sigma - \sigma_d}\right)^2$ for a channel flow.

Noteworthy is the (quadratic) dependence of the Babel number on the stress gradient, i.e., the pressure gradient in a Poiseuille flow. Indeed, it is generally several orders of magnitude larger in microchannels than in their larger counterparts, which explains why striking manifestations of cooperativity have been observed only in the former. The Babel number is also negligible in wide-gap Taylor-Couette geometry. For instance, a rough estimation yields $\text{Ba} \sim 10^{-9}$ at most in the wide-gap setup used by Ovarlez et al.⁵³, where no deviations from macroscopic rheology were reported.

The denominator of Ba, $(\sigma - \sigma_d)^2$, also deserves a comment: at high applied stresses, when the material is more fluid-like, relative deviations become less significant. We should however say that, to measure relative deviations, the absolute fluidity deviations are divided by the fluidity, which gets large as σ gets large.

4.2 Nonlocal effects in the velocity profiles

Following the above considerations, we expect deviations from macroscopic rheology to increase with confinement, at fixed wall stress.

Indeed, Goyon's experiments on emulsions confined in microchannels with *smooth* walls tend to indicate that the deviations of the velocity with respect to the bulk predictions follow such a trend. However, overall, these deviations were found to be rather small. The mentioned effect of confinement is also confirmed by Chaudhuri et al. with atomistic simulations of a Poiseuille flow with biperiodic boundary conditions with atomistic simulations⁴⁰.

Figure 9 shows a comparison between the actual velocity profile obtained with simulations of the mesoscopic model and the predictions from the (bulk) flow curve. As in experiments, small deviations can be observed. For the extent of these deviations to roughly match that in the experiments, the channel width must be of order 7-10 block units. From this we deduce a first estimate for the linear size N_{\varnothing} of a mesoscopic block in terms of particle diameters: $N_{\varnothing} \approx 2$, which is comparable to experimental values found in the literature³⁵.

Let us now investigate how compatible our simulation results are with the fluidity diffusion equation, Eq. 14. To solve Eq. 14, two boundary conditions are required: for symmetry reasons, we impose $f(y=0) = f(y=L_y)$, and we set the fluidity at a point close to the wall to the value measured in simulations. In addition, the shear-rate dependence of the cooperativity length ξ must be specified. Two possibilities are considered in Fig. 10: either, following Goyon *et al.*³⁹, ξ is supposed independent of the shear rate, i.e., $\xi = \xi_0$, or a power-law dependence is assumed, $\xi(\dot{\gamma}) = \xi_0 (\dot{\gamma}\tau)^{-1/4}$, where $\dot{\gamma}$ is the product of the local shear stress and fluidity, as derived in Ref.¹⁶ in the limit $\dot{\gamma} \rightarrow 0$, and in reasonable agreement with the data of Ref.⁴⁵. In both cases, ξ_0 is adjusted by a least square minimization. Both cases give a reasonable fit, but neither matches our data accurately over the whole range of applied pressures. We ascribe this defect, among other details, to the approximation of long-range interactions by a diffusive term, and to the neglect of fluidity fluctuations.

In Figure 11, we assess the predictive capability of the theoretically derived Babel number for our channel flow simulations by plotting the $\frac{\delta f}{f}$ obtained in our simulations as a function of $Ba = \left(\xi \frac{\|\nabla\sigma\|}{\sigma - \sigma_d}\right)^2$. It shows a global trend towards larger relative deviations from macroscopic rheology for larger Ba, but the correlations are poor. Nevertheless, one may expect Ba to still be a valid predictor in practice, when widely different situations are considered.

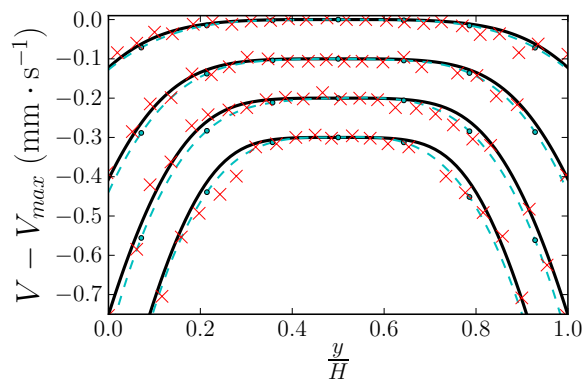


Fig. 9 Velocity profiles across the channel, for $\sigma_w = 45, 60, 75, 91$ Pa, i.e., $\sigma_w = 0.75, 1.0, 1.25, 1.52$ in model units, from top to bottom: (dashed line) simulation results, (solid line) predictions based on the numerical bulk flow curve. The crosses are experimental data obtained by Goyon *et al.*⁴⁴. Note that the curves have been shifted with respect to each other for clarity.

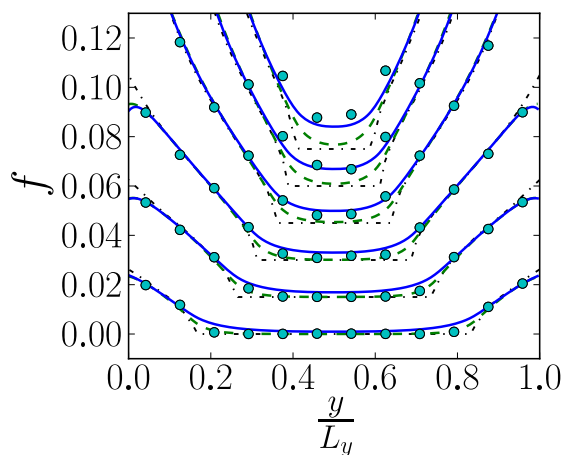


Fig. 10 Fluidity profiles for $N_y = 12$, for $\sigma_w = 0.20, 0.28, 0.36, 0.48, 0.60, 0.72$ in model units. Filled circles: numerical results, dashed green line: solution of Eq.14 with $\xi(\dot{\gamma}) = 0.03702$, solid blue line: solution of Eq.14 with $\xi(\dot{\gamma}) = 0.01146\dot{\gamma}^{-0.25}$. The thin dash-dotted lines represent the bulk fluidity f_{bulk} . Note that the curves are shifted with respect to each other for clarity.

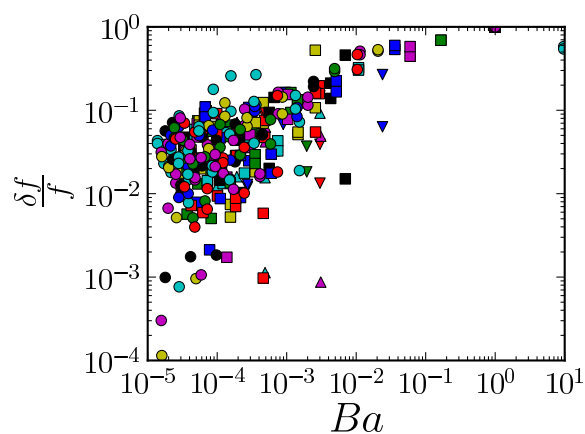


Fig. 11 Relative deviations $\frac{\delta f}{f}$ of the local fluidity f from the bulk fluidity $f_{\text{bulk}}(\sigma)$ measured in simulations, where σ is the local shear stress, as a function of the estimated Babel number $Ba = \left(\xi_0 \frac{\sqrt{\sigma}}{\sigma - \sigma_d}\right)^2$. We have set ξ_0 to 0.037 (see Fig.10). Data only include regions where $\sigma > \sigma_d$, but cover various applied pressures and channel widths: (\blacktriangledown) 6 blocks, (\blacktriangle) 10 blocks, (\blacksquare) 16 blocks, (\bullet) 24 blocks.

4.3 Shear rate fluctuations in the plug

Quite recently, Jop and co-workers⁴⁵ showed experimentally that the seemingly quiescent plug in the centre of the microchannel actually sustains finite shear rate fluctuations. This observation is obviously consistent with the occurrence of sparse plastic events in the plug, in our simulations.

To go further than this qualitative agreement, we directly compare the local shear rate fluctuations $\delta\dot{\gamma}(x,y) = \sqrt{\langle \dot{\gamma}(x,y)^2 \rangle - \langle \dot{\gamma}(x,y) \rangle^2}$ to experimental data[§], with the parameters used to fit the associated velocity profiles (see Fig.9). Here, $\dot{\gamma}(x,y)$ is the local shear rate at point (x,y) ; it is given by $\dot{\gamma}(x,y) = 2 \left(\dot{\epsilon}_{xy}^{pl}(x,y) + \dot{\epsilon}_{xy}^{(1)}(x,y) \right)$ in the model and is therefore obtained directly, that is, without deriving the velocity with respect to space. Figure 12 presents the experimental shear rate fluctuation profiles and their numerical counterparts for $N_y = 16$ blocks crosswise. Semi-quantitative agreement is observed in regions far from the walls - apart from the large discrepancy at the highest applied pressure. The discrepancies in the highly-sheared regions near the walls will be considered below. It is interesting to note that the fitted channel size provides another estimate for the size N_{ϕ} of an elastoplastic block, which agrees with the first one, $N_{\phi} \approx 2$. Figure 13 shows the dependence of the shear rate fluctuations on the channel size for a given stress at the wall. As expected from the expression of the Babel number, fluctuations in the plug decay when the channel width is increased.

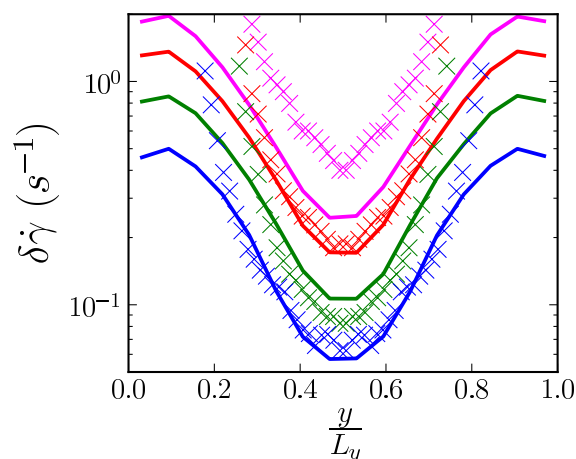


Fig. 12 Shear rate fluctuations $\delta\dot{\gamma}(y)$ (averaged along the x -direction), for $\sigma_w = 141$ Pa, 188 Pa, 235 Pa, 282 Pa (identical to Fig.6), from bottom to top. (×) Experimental data collected by Jop *et al.*⁴⁵, (solid lines) numerical results for $N_y = 16$.

§ Note that we have discarded the two curves corresponding to the lowest applied pressures, which seem to plateau in the centre, because we were not entirely sure of the accuracy of these measurements.

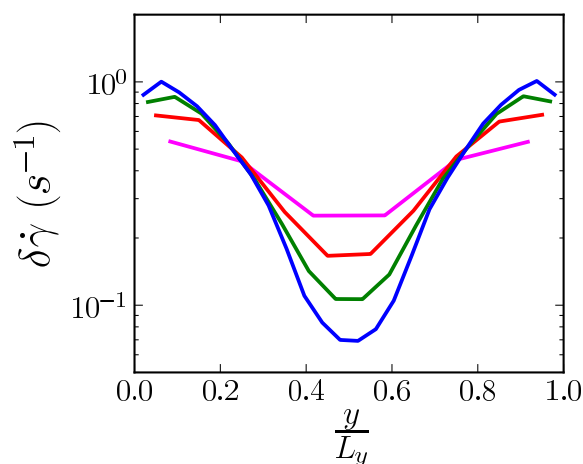


Fig. 13 Shear rate fluctuation profiles for a given stress at the wall, $\sigma_w = 0.48$ in model units, for different channel widths: (fuchsia) 6, (red) 10, (green) 16, and (blue) 24 blocks, in descending order of minimal values.

Let us note that the data collected by Jop and co-workers suggested a proportionality between the shear rate fluctuations and the local fluidity, implying that both are indicators of the intensity of the plastic activity. Figure 14 shows that the line-averaged plastic activity does indeed depend linearly on the local fluidity in our channel flow simulations, despite some discrepancies at low values of the fluidity, that is, probably in the plug. However, the relation between the shear rate fluctuations and the mean fluidity is much less clear (see Fig.15).

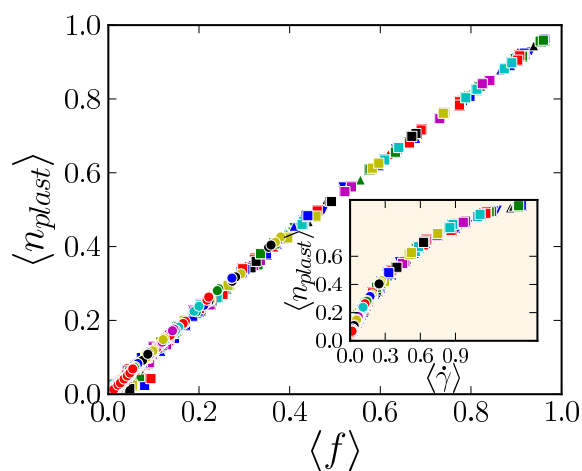


Fig. 14 Time-averaged fraction of plastic blocks $\langle n_{plast} \rangle$ on a given streamline as a function of the mean fluidity $\langle f \rangle$ on that line, for diverse applied pressures and various channel widths: (\blacktriangledown) 6 blocks, (\blacktriangle) 10 blocks, (\blacksquare) 16 blocks, (\bullet) 24 blocks. *Inset:* $\langle n_{plast} \rangle$ vs. the mean shear rate $\langle \dot{\gamma} \rangle$ on the line. (Same symbols).

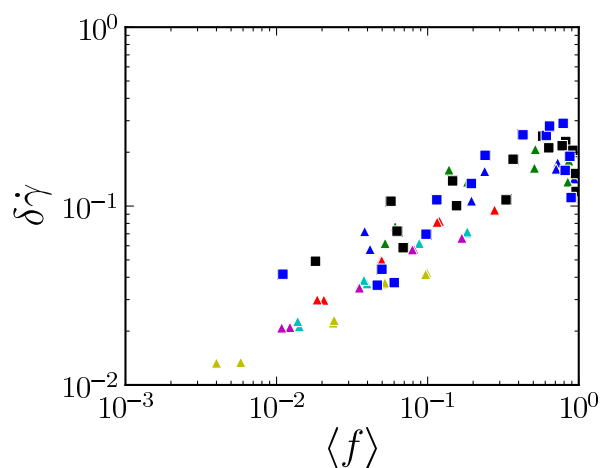


Fig. 15 Shear rate fluctuations $\delta\dot{\gamma}$ on a given streamline as a function of the mean fluidity $\langle f \rangle$ on that line, for diverse applied pressures and various channel widths: (\blacktriangle) 8 blocks, (\blacksquare) 16 blocks, (\bullet) 24 blocks.

5 A specific rheology near the walls?

In the previous section, we have dealt with the flow cooperativity associated with the coupling of heterogeneous streamlines, leaving aside another potentially significant difference with bulk homogeneous flow: the presence of walls bounding the flow, which is known to affect the flow of diverse complex fluids: wormlike micellar solutions^{54,55}, laponite⁵⁶, dense colloidal suspensions⁴⁷, etc. Indeed, Goyon et al. provided experimental evidence of the occurrence of ample changes when rough walls are substituted for smooth walls³⁹. Then, much larger deviations from bulk rheology are observed, especially at high applied pressures, and these deviations are maximal close to the walls, contrary to predictions based on the Babel number.

5.1 Weak deviations due to no slip boundary condition

Remember that walls are described by a no-slip boundary condition in our model. This condition results in a significantly larger dissipation during plastic events in their vicinity. Is this sufficient to capture the very large deviations observed experimentally?

Figure 16 shows the local flow curve for the simulations. To decouple to a certain extent the problem of wall rheology from the inhomogeneous driving, the latter being associated with large values of Ba , a relatively large channel is considered here. For each value of the wall stress, the points with the highest local shear rates in Fig.16 are closest to the walls. We do observe some slight deviations[¶], but they are clearly much weaker than in Goyon's observations (see Fig.6

[¶] Nevertheless, replacing the no slip boundary condition with a periodic boundary condition will play a role if the Babel number is large enough. See Ref.⁴⁰ for the effect of confinement on the observed yield stress in a biperiodic Poiseuille flow.

of Ref.⁴⁴ for instance). In this respect, they much better describe the situation for smooth walls, which, at first, might seem surprising given the no-slip boundary conditions. Yet, in reality, the large slip observed at smooth walls is not expected to give rise to significant changes: it only adds a simple global translation to the complex velocity field obtained with no-slip boundary conditions.

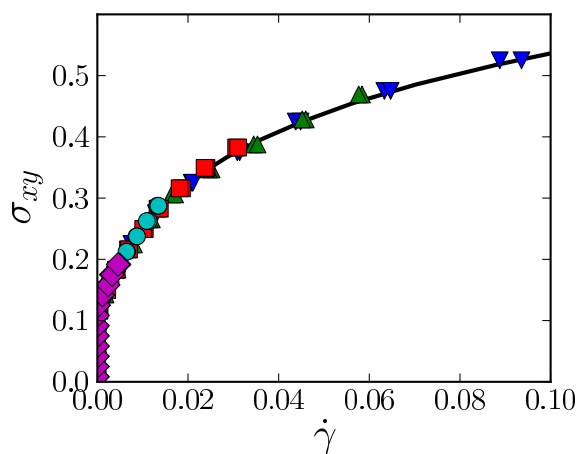


Fig. 16 Local shear stress as a function of the local shear rate, for various applied pressures for a channel width of 24 blocks. The corresponding stresses at the walls are: (purple rhombs) $\sigma_w = 0.2$, (cyan dots) $\sigma_w = 0.2$, (red squares) $\sigma_w \approx 0.4$, (green upper triangles) $\sigma_w \approx 0.5$, (blue lower triangles) $\sigma_w = 0.6$.

5.2 Physical effect of rough walls

As the deviations observed for rough walls are not captured by a simple no slip boundary condition, we discuss here some physical mechanisms that may be responsible for the observed behaviour.

First, the static structure near walls is known to differ from that in the bulk. For smooth, or not too rough, boundaries, stratification in layers is often reported over a distance of a few particle diameters^{57,58}, though not systematically: Goyon et al.⁴⁴ actually observed no such layering in their experiments. Besides, the vicinity of a solid boundary hinders the mobility of Brownian particles⁵⁹. But these structural changes for the material at rest imply a decrease of the fluidity at the wall, as opposed to the enhancement that is experimentally observed by Goyon³⁹ and Géraud⁴⁶ at high enough stresses, i.e., where the largest deviations occur. Alternatively, the specific behaviour at the wall is often rationalised by the existence of a depleted 'lubrication layer' close to the wall, as is often found in sheared dispersions^{60–66}. This phenomenon is more acute for deformable particles⁶² undergoing high shear rates and/or high shear gradients; it generates an apparent wall slip. However, at the very high concentrations investigated here, owing to the large osmotic pressure, such a lubricating layer would have a thickness of order 100 nm or less^{44,65,66} (if the lubricating layer is composed of pure solvent). Effectively, Goyon directly measured the concentration profile across

the channel and was not able to detect any significant variation. This finding is corroborated by the absence of radial droplet migration for a similar material in a Taylor-Couette cell, even at high shear rates, as reported by Ovarlez et al.⁵³. Adding that systems of soft particles have a much weaker viscosity dependence on concentration than their hard particle counterparts, effects of concentration variations could be ruled out as regards Goyon's experiments. Nevertheless, we attempted to simulate a less viscous layer close to the wall by decreasing the yield stress of the associated mesoscopic blocks, but this only had little effect on the rest of the system. Therefore, one is led to seek another explanation.

An aspect that has been overlooked so far is the reported observation of wall slip in Goyon's, Geraud's and Jop and Mansard's works^{39,44,46,58}, both with smooth and rough walls. In order to extract information that is relevant for the bulk flow, the authors measured the *local* velocities and shear rates in the channel by microscopic observation, so that the occurrence of slippage should *a priori* not affect their results. Indeed, in presence of smooth surfaces, where wall slip accounts for around 30% of the maximal velocity at the typical pressures applied by Goyon et al.³⁹, slip only results in a global translation of the system, that leaves the local flow curve strictly unaltered. For rough surfaces, let us first remark that the presence of wall slip is more surprising, since roughened surfaces^{||} are often used to strongly suppress, or eliminate, slip for the very same type of materials, which is monitored by rheological measurements, and then used as benchmarks for a system without slip^{61,64,67–69}. However, in several cases, measurements of local velocities in the flow, either with microvelocimetry with fluorescent tracers^{44,46,70} or through direct visualisation with confocal microscopy^{45,58}, demonstrate that concentrated emulsions may slip along rough surfaces in microchannels. A seemingly quadratic^{46,70}, or linear⁵⁸, dependence of the slip velocity on the shear stress at the wall is reported in these cases. As a side note, let us add that slip along a rough wall is not restricted to the microchannel geometry: for instance, Divoux *et al.* showed with ultrasonic speckle velocimetry that another yield stress fluid, namely carbopol, experiences a phase of total slip in a Taylor-Couette rheometer whose cylinders had been coated with sand paper⁷¹.

Now, when particles slide along a rough wall, they are expected to bump into, and be deformed by, the surface asperities. In the case of asperities that are large as compared to the "particle" size (~ 60 microns *vs.* from a few to 20 microns), this phenomenon is best exemplified by the spatiotemporal diagram acquired with ultrasonic velocimetry for a carbopol microgel, Fig.6 of Ref.⁷², where one can see a large deformation of the material that originates at the rotor and propagates almost instantaneously into the bulk; this signal was interpreted by the authors as the signature of a "bump" into a surface protuberance. Albeit less visible, this effect should also appear with walls characterised by a smaller roughness, whereby rough walls in the presence of slip act as sources of mechanical noise and cause deviations from bulk rheology in their vicinity. This tentative scenario has the potential to explain why deviations may, or may not, be observed in the vicinity of rough surfaces: for instance, Goyon et al.⁴⁴ and Ovarlez et al.⁵³, as well as Seth and co-workers⁷³, have reported that the local flow curves obtained

|| Diverse methods are available for roughening a surface, such as sandblasting, covering it with sandpaper, or coating it with particles.

in wide gap Taylor-Couette or plate-plate geometries with rough walls could be mapped onto the macroscopic flow curves; yet, they also indicated that, in those cases, no evidence of wall slip could be found. Very recently, Mansard endeavoured to investigate the impact of wall roughness by combining experiments and molecular dynamics simulations⁵⁸. Nonmonotonic variations of the wall fluidity as a function of the roughness were reported in the experiments, but the data did not allow for the extraction of the parameters responsible for the deviations from macroscopic rheology. Nevertheless, he noted that “the particles must jump over the patterns [on the walls]. This effect induces the rearrangements and increases the wall fluidity”.

Naturally, this prompts the following question: what determines the occurrence of slip along rough walls? This question lies far beyond the scope of the present study. Let us simply note that in Refs.^{39,44–46} the size of surface asperities was a couple of microns at most, that is, significantly less than the typical “particle” size, which plausibly favours slip, as well as the high shear rates experienced at the microchannel walls. Nevertheless, recent theories of slip along smooth walls involved, in addition, parameters such as the deformability of the droplets,^{63,64} and the particle-wall interactions⁷⁴, not to mention the presumably significant impact of Brownian motion in cases where it is relevant^{75,76}. As far as we know, the somewhat daunting challenge to extend these theories to the case of rough walls still awaits a successful accomplisher.

In the above discussion, we have carefully eluded the question of the surface chemistry and its interactions with the particles. However, Seth and co-workers showed that they can play a significant role; in particular, for the yield stress fluid they studied, smooth attractive surfaces were observed to induce deviations from macroscopic rheology relatively far into the bulk, whereas smooth repulsive induced none at all.

Finally, we would like to mention another possible impact of the confinement of the material between walls. The channel may be so narrow that the layers where the specific wall rheology dominates start overlapping. This situation, which is described as strong confinement, is expected to occur when the channel width becomes of the order of, or smaller than, the cooperativity length ξ . For the data of Refs.^{39,44,45} discussed above, this mechanism is therefore not relevant.

5.3 Fictitious plastic events along the wall as mechanical noise sources

As we have already noted, nonlocal effects leading to deviations from the macroscopic flow curve are often rationalised in terms of the fluidity diffusion equation, Eq.14 (see, e.g., Ref.^{39,40,44–46,52,58,73}). In this approach, the fluidity at the wall is needed as an input parameter, whose precise value turns out to be determinant. Most likely, the suggested mechanical noise at the walls would be hidden in that value. (Note that, in Goyon⁷⁰ the fluidity at rough walls, where larger deviations are observed, is indeed larger than that for smooth walls and larger than the bulk fluidity corresponding to the same shear stress.)

Our mesoscopic model is also oblivious to the microscopic details of the flow near a boundary and therefore cannot describe the effect of wall slip along a rough wall without further input. Nevertheless, since bumps act as sources of mechanical noise in the system, one can attempt to account for their occurrence

by adding fictitious plastic events along the walls. Note that this ad hoc treatment is similar to imposing a wall fluidity larger than the bulk fluidity as a boundary condition when solving the fluidity diffusion equation, Eq. 14.

More precisely, we modify the implementation of the model slightly, so that a wall is now described as a line of plastically inert blocks: the bottom wall will, for instance, occupy the portion of space $0 \leq y \leq 1$, and the no slip boundary condition is imposed at its centre, i.e., $y = 0.5$. On this line, a fraction of blocks is selected** at random to act as sources of mechanical noise, that is, to mimic, e.g., bumps of particles into surface asperities. To do so, they shall release a constant plastic strain $\dot{\epsilon}_{fict}^{pl}$ per unit time, along the direction of macroscopic shear (for simplicity). We emphasise that mechanical equilibrium is not violated by the addition of these fictitious plastic events.

Figure 17 shows the local flow curves obtained with this protocol. The observed deviations are qualitatively similar to those reported by Goyon (see Fig.7 of Ref.⁴⁴). However, we must note that a rather intense mechanical noise is required to get such deviations ($\dot{\epsilon}_{fict}^{pl} \approx 5$). (As the value of $\dot{\epsilon}_{fict}^{pl}$ is arbitrary, we do not seek quantitative agreement with the experimental data here). In addition, these fictitious plastic events also alter the shear rate fluctuation profile, as shown in Fig. 18. Besides, a global increase of the fluctuations, the profile no longer flattens in the vicinity of the walls, which renders it more consistent with the experimental results of Jop and co-workers (collected in a channel with rough walls).

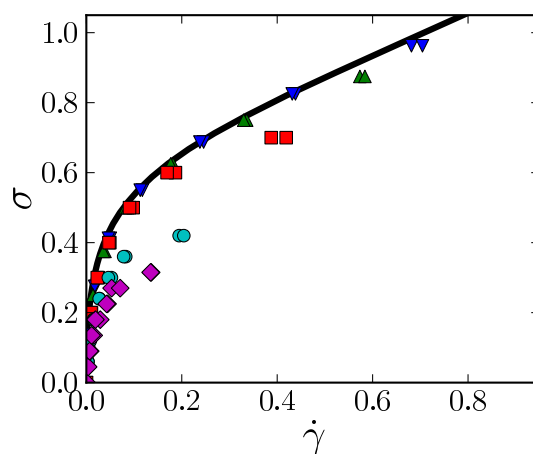


Fig. 17 Local shear rate $\sigma(y)$ vs local shear rate $\dot{\gamma}(y)$ (averaged on streamlines $y = cst$) in the microchannel, when fictitious mechanical noise sources of intensity $\dot{\epsilon}_{xy}^{fict pl} = \pm 4.5$ are added on a fraction ($1/3$) of blocks on the wall lines. $\sigma_w =$ (♦) 0.36, (●) 0.48, (■) 0.8, (▲) 1.0, (▼) 1.1 in model units. Solid line: macroscopic flow curve.

** Note that shuffling these blocks, i.e., selecting new random blocks as noise sources, at low enough frequency hardly affects the results presented below.

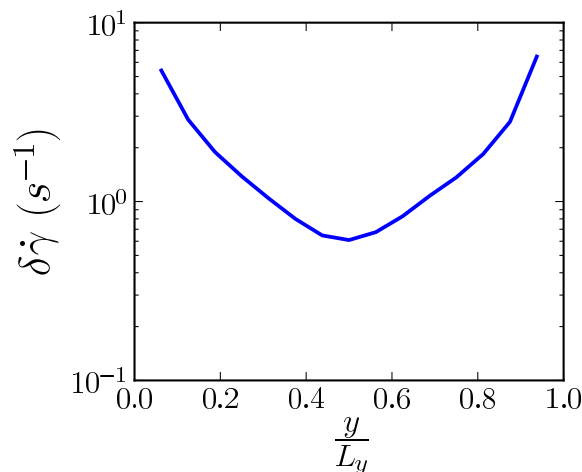


Fig. 18 Shear rate fluctuation profiles in the presence of fictitious plastic events along the walls. A third of the blocks on wall lines have been randomly selected to release a constant plastic stress $\sigma_{xy}^{pl\,fict} = 4.5$ per unit time.

6 Conclusions & Outlook

In conclusion, we have derived analytical formulae from continuum mechanics for the effect and time evolution of a plastic event occurring in a two dimensional medium bounded by walls. We have integrated these formulae in a lattice model for the flow of amorphous solids, in which elastoplastic blocks receive stress from their surroundings and have a certain probability to become plastic; the chosen form of probabilities for the onset and end of a plastic event allowed us to match experimental flow curves for concentrated emulsions. Then we turned to the simulation of flow in microchannels, where the most prominent feature is the existence of a seemingly unsheared “plug”. Remarkable manifestations of spatial cooperativity in the flow had been unveiled experimentally, and we proposed to distinguish those pertaining to cooperativity in the bulk from those pointing to the specific rheology near a solid boundary. For the former category, deviations of time averaged quantities are generally weak, but could nevertheless be observed with our model. More strikingly, shear rate fluctuations were observed in the plug, consistently with experiments. As regards the specific wall rheology, it turned out that imposing no-slip boundary conditions at the walls in our model was not sufficient to capture the experimentally observed phenomena. We discussed several possible physical origins for the departure from the macroscopic behaviour observed, above all, in the vicinity of rough surfaces; we insisted in particular on a tentative scenario in which mechanical noise is created at the wall by, e.g., bumps of particles into surface asperities as they slide along the wall. Finally, an ad hoc implementation of this mechanical noise was attempted.

Concerning our mesoscopic model, several improvements can be considered. First and foremost, regions undergoing plastic events are fluidised, and the presence of fluid-like regions is expected to damp shear waves and reduce cooperativity. This point is not taken into account in the model. Also, the distinction

between an activation temperature, of noncooperative origin, and a more general effective temperature will be worth further investigation, both for thermal and 'athermal' soft solids under shear. In an unrelated way, it has been apparent that, in spite of the vast amount of literature on the question of slip for soft solids and the recent progress made in that respect⁶³, the issue of slip along a rough surfaces, and its consequences on the local fluidity, remains quite challenging.

Acknowledgments.

We thank T. Divoux, K. Martens, P. Chaudhuri, S. Manneville, and M. Fardin for interesting discussions. JLB is supported by Institut Universitaire de France and by grant ERC-2011-ADG20110209.

References

- 1 L. Berthier, G. Biroli, J.-P. Bouchaud, L. Cipelletti, D. El Masri, D. L'Hôte, F. Ladieu and M. Pierno, *Science (New York, N.Y.)*, 2005, **310**, 1797–800.
- 2 C. Heussinger, P. Chaudhuri and J.-L. Barrat, *Soft matter*, 2010, **6**, 3050–3058.
- 3 D. Rodney, A. Tanguy and D. Vandembroucq, *Modelling and Simulation in Materials Science and Engineering*, 2011, **19**, 083001.
- 4 K. A. Dahmen, Y. Ben-Zion and J. T. Uhl, *Nature Physics*, 2011, **7**, 554–557.
- 5 A. Argon and H. Kuo, *Materials Science and Engineering*, 1979, **39**, 101–109.
- 6 A. Lemaître and C. Caroli, *Physical Review E*, 2007, **76**, 036104.
- 7 M. Tsamados, A. Tanguy, F. Léonforte and J.-L. Barrat, *The European physical journal. E, Soft matter*, 2008, **26**, 283–93.
- 8 M. Falk and J. Langer, *Physical Review E*, 1998, **57**, 7192.
- 9 M. L. Falk and J. S. Langer, *ANNUAL REVIEW OF CONDENSED MATTER PHYSICS, VOL 2*, 2011, vol. 2, pp. 353–373.
- 10 P. Sollich, F. Lequeux, P. Hébraud and M. Cates, *Physical Review Letters*, 1997, **78**, 2020–2023.
- 11 P. Sollich, *Physical Review E*, 1998, **58**, 738.
- 12 P. Hébraud and F. Lequeux, *Physical Review Letters*, 1998, **81**, 2934–2937.
- 13 P. Coussot, Q. Nguyen, H. Huynh and D. Bonn, *Physical Review Letters*, 2002, **88**, 175501.
- 14 M. Manning, J. Langer and J. Carlson, *Physical Review E*, 2007, **76**, 056106.
- 15 S. M. Fielding, M. E. Cates and P. Sollich, *Soft Matter*, 2009, **5**, 2378.
- 16 L. Bocquet, A. Colin and A. Ajdari, *Physical Review Letters*, 2009, **103**, 036001.
- 17 K. Chen, P. Bak and S. Obukhov, *Physical Review A*, 1991, **43**, 625–630.
- 18 V. V. Bulatov and A. S. Argon, *Modelling and Simulation in Materials Science and Engineering*, 1994, **2**, 167–184.
- 19 V. V. Bulatov and A. S. Argon, *Modelling and Simulation in Materials Science and Engineering*, 1994, **2**, 185–202.

-
- 20 V. V. Bulatov and A. S. Argon, *Modelling and Simulation in Materials Science and Engineering*, 1994, **2**, 203–222.
 - 21 J.-C. Baret, D. Vandembroucq and S. Roux, *Physical Review Letters*, 2002, **89**, 195506.
 - 22 G. Picard, A. Ajdari, F. Lequeux and L. Bocquet, *Physical Review E*, 2005, **71**, 010501.
 - 23 E. R. Homer and C. A. Schuh, *Acta Materialia*, 2009, **57**, 2823–2833.
 - 24 K. Martens, L. Bocquet and J.-L. Barrat, *Soft Matter*, 2012, 4197.
 - 25 K. Martens, L. Bocquet and J.-L. Barrat, *Physical Review Letters*, 2011, **106**, 156001.
 - 26 A. Nicolas and J.-L. Barrat, *Physical Review Letters*, 2013, **110**, 138304.
 - 27 H. Princen, *Journal of Colloid and Interface Science*, 1985, **105**, 150–171.
 - 28 C. Maloney and A. Lemaître, *Physical Review E*, 2006, **74**, 016118.
 - 29 A. Amon, V. Nguyen, A. Bruand, J. Crassous and E. Clément, *Physical Review Letters*, 2012, **108**, 135502.
 - 30 M. Le Merrer, S. Cohen-Addad and R. Höhler, *Physical Review Letters*, 2012, **108**, 188301.
 - 31 J. Bouchaud and E. Pitard, *The European Physical Journal E*, 2001, **6**, 231–236.
 - 32 M. Cloitre, R. Borrega, F. Monti and L. Leibler, *Physical Review Letters*, 2003, **90**, 068303.
 - 33 G. Picard, A. Ajdari, F. Lequeux and L. Bocquet, *The European physical journal. E, Soft matter*, 2004, **15**, 371–81.
 - 34 F. Leonforte, R. Boissière, A. Tanguy, J. Wittmer and J.-L. Barrat, *Physical Review B*, 2005, **72**, 224206.
 - 35 P. Schall, D. A. Weitz and F. Spaepen, *Science (New York, N.Y.)*, 2007, **318**, 1895–9.
 - 36 J. Bokeloh, S. V. Divinski, G. Reglitz and G. Wilde, *Physical Review Letters*, 2011, **107**, 235503.
 - 37 R. Besseling, L. Isa, P. Ballesta, G. Petekidis, M. Cates and W. Poon, *Physical Review Letters*, 2010, **105**, 268301.
 - 38 M. Talamali, V. Petäjä, D. Vandembroucq and S. Roux, *Comptes Rendus de Mécanique*, 2012, **340**, 275.
 - 39 J. Goyon, A. Colin, G. Ovarlez, A. Ajdari and L. Bocquet, *Nature*, 2008, **454**, 84–7.
 - 40 P. Chaudhuri, V. Mansard, A. Colin and L. Bocquet, *Physical Review Letters*, 2012, **109**, 036001.
 - 41 O. Pouliquen, Y. Forterre and S. Le Dizes, *Advances in Complex Systems*, 2001, **04**, 441–450.
 - 42 R. R. Hartley and R. P. Behringer, *Nature*, 2003, **421**, 928–31.
 - 43 A. Amon, R. Bertoni and J. Crassous, 2012.
 - 44 J. Goyon, A. Colin and L. Bocquet, *Soft Matter*, 2010, **6**, 2668.
 - 45 P. Jop, V. Mansard, P. Chaudhuri, L. Bocquet and A. Colin, *Physical Review Letters*, 2012, **108**, 148301.
 - 46 B. Geraud, L. Bocquet and C. Barentin, *The European physical journal. E, Soft matter*, 2013, **36**, 9845.

-
- 47 L. Isa, R. Besseling and W. C. K. Poon, *Physical Review Letters*, 2007, **98**, 198305.
- 48 L. Isa, R. Besseling, A. Morozov and W. Poon, *Physical Review Letters*, 2009, **102**, 058302.
- 49 O. Pouliquen and R. Gutfraind, *Physical Review E*, 1996, **53**, 552.
- 50 R. Gutfraind and O. Pouliquen, *Mechanics of materials*, 1996, **24**, 273–285.
- 51 J.-B. Salmon, L. Bécu, S. Manneville and A. Colin, *The European Physical Journal E*, 2003, **10**, 209–221.
- 52 K. Kamrin and G. Koval, *Physical Review Letters*, 2012, **108**, 178301.
- 53 G. Ovarlez, S. Rodts, A. Ragouilliaux, P. Coussot, J. Goyon and A. Colin, *Physical Review E*, 2008, **78**, 036307.
- 54 C. Masselon and A. Colin, *Physical Review E*, 2010, **81**, 021502.
- 55 L. Bécu, S. Manneville and A. Colin, *Physical Review Letters*, 2004, **93**, 018301.
- 56 T. Gibaud, C. Barentin and S. Manneville, *Physical Review Letters*, 2008, **101**, 258302.
- 57 P. Ballesta, R. Besseling, L. Isa, G. Petekidis and W. Poon, *Physical Review Letters*, 2008, **101**, 258301.
- 58 V. Mansard, *PhD thesis*, Université de Bordeaux I, 2012.
- 59 E. Pagac, R. Tilton and D. Prieve, *Chemical engineering communications*, 1996, **148**, 105–122.
- 60 A. Yoshimura and R. K. Prud'homme, *Journal of Rheology*, 1988, **32**, 53.
- 61 H. A. Barnes, *Journal of Non-Newtonian Fluid Mechanics*, 1995, **56**, 221–251.
- 62 J. Franco, C. Gallegos and H. Barnes, *Journal of Food Engineering*, 1998, **36**, 89–102.
- 63 S. Meeker, R. Bonnecaze and M. Cloitre, *Physical Review Letters*, 2004, **92**, 198302.
- 64 S. P. Meeker, R. T. Bonnecaze and M. Cloitre, *Journal of Rheology*, 2004, **48**, 1295.
- 65 J.-B. Salmon, A. Colin and S. Manneville, *Physical Review Letters*, 2003, **90**, 228303.
- 66 L. Bécu, P. Grondin, A. Colin and S. Manneville, *Colloids and Surfaces A: Physicochemical and Engineering Aspects*, 2005, **263**, 146–152.
- 67 T. Mason, J. Bibette and D. Weitz, *Journal of Colloid and Interface Science*, 1996, **179**, 439–448.
- 68 M. Sanchez, C. Valencia, J. Franco and C. Gallegos, *Journal of colloid and interface science*, 2001, **241**, 226–232.
- 69 G. H. Meeten, *Journal of non-newtonian fluid mechanics*, 2004, **124**, 51–60.
- 70 J. Goyon, *PhD thesis*, Université de Bordeaux I, 2008.
- 71 T. Divoux, C. Barentin and S. Manneville, *Soft Matter*, 2011, **7**, 9335–9349.
- 72 T. Divoux, C. Barentin and S. Manneville, *Soft Matter*, 2011, **7**, 8409–8418.
- 73 J. R. Seth, C. Locatelli-Champagne, F. Monti, R. T. Bonnecaze and M. Cloitre, *Soft Matter*, 2012, **8**, 140.
- 74 J. R. Seth, M. Cloitre and R. T. Bonnecaze, *Journal of Rheology*, 2008, **52**, 1241.

- 75 R. Besseling, L. Isa, E. R. Weeks and W. C. Poon, *Advances in colloid and interface science*, 2009, **146**, 1–17.
- 76 P. Ballesta, G. Petekidis, L. Isa, W. C. K. Poon and R. Besseling, *Journal of Rheology*, 2012, **56**, 1005.
- 77 I. Gradshteyn and I. Ryzhik, *Tables of Integrals, Series and Products*, (edited by A. Jeffrey), 1994.

Appendices

A Derivation of the correction terms to the propagator for a system bounded by walls

The system covers the domain $(x, y) \in [0, L_x] \times [-L_y, L_y]$ and is periodically replicated throughout space. The region $y \in [0, L_y]$, bounded by walls at $y = 0$ and $y = L_y$ represents the *real* system, whereas the other half is a fictitious region introduced for the calculations.

For any plastic event $\varepsilon^{pl} = (\varepsilon_{xx}^{pl}, \varepsilon_{xy}^{pl})^T$ occurring at position (x, y) in the real half, a 'symmetric' plastic event $\varepsilon^{pl'} = (\varepsilon_{xx}^{pl}, -\varepsilon_{xy}^{pl})^T$ is created at location $(x, -y)$ in the fictitious region. For symmetry reasons, the y -component of the velocity field is thereby cancelled on lines $y = 0$ and $y = L_y$ (bear in mind that the $2L_y$ -wide system is periodically replicated).

Let us now introduce forces $f_x^{(y=0)}$ and $f_x^{(y=L_y)}$ along the x -direction at the bottom ($y = 0$) and top ($y = L_y$) walls, respectively, to cancel the x -components. The Fourier transform of the force field reads:

$$f_x(m, n) = f_x^{(y=0)}(m) + (-1)^n f_x^{(y=L_y)}(m)$$

Note that we have simplified notations by using the shorthand $g(m, n)$ for $\hat{g}(p_m, q_n)$, for any function g , where $p_m \equiv \frac{2\pi}{L_x}$ and $q_n \equiv \frac{2\pi}{2L_y}$ are the Fourier wavenumbers.

With these forces, the Fourier-transformed displacement field turns into:

$$\begin{aligned} u^{(1)}(m, n) &= \mathcal{G}^\infty(m, n) \cdot (\hat{\varepsilon}^{pl}(m, n) + \hat{\varepsilon}^{pl'}(m, n)) + O(m, n) \cdot f_x(m, n) \\ &\equiv u^{*\infty}(m, n) + u^{corr}(m, n), \end{aligned} \quad (16)$$

where \hat{u}^{corr} is the contribution from the wall forces and \hat{O} is the Oseen-Burgers tensor introduced in Eq. 8. The star in $\hat{u}^{*\infty}$ only indicates that this symbol represents the velocity field induced by both the real plastic event and its 'symmetric' counterpart.

Remarking that the condition of zero velocity at the bottom and top walls reads, in terms of Fourier components,

$$\begin{aligned} \forall m, \sum_n u^{(1)}(m, n) &= 0 \\ \text{and } \forall m, \sum_n (-1)^n u^{(1)}(m, n) &= 0, \end{aligned}$$

respectively, we obtain two equations on the f_x after insertion from Eq.15. Adding and subtracting these equations yields, for any m :

$$\sum_{n \in O} u_x^{*\infty}(m, n) + O(m, n) \cdot \left(\left(\hat{f}_x^{(y=0)} - \hat{f}_x^{(y=L_y)} \right) (m) \right) = 0$$

$$\sum_{n \in E} u_x^{*\infty}(m, n) + O(m, n) \cdot \left(\left(\hat{f}_x^{(y=0)} + \hat{f}_x^{(y=L_y)} \right) (m) \right) = 0$$

where $O \equiv 2\mathbb{Z} + 1$ is the set of odd integers, and $E \equiv 2\mathbb{Z}$ is the set of even integers.

The solution of this linear system of equations is:

$$f(m \neq 0, n \in \delta) = \frac{-\mu}{e_\delta(m)} \sum_{n' \in \delta} u_x^{*\infty}(m, n'), \quad (17)$$

where the symbol δ stands for either E (even n 's) or O (odd n 's). The expressions for $m = 0$ are written separately:

$$f(0, n \in 2\mathbb{Z}) = 0$$

$$f(0, n \in O) = \frac{-4\mu}{L_y^2} \sum_{n' \in O} u_x^{*\infty}(m, n').$$

In Eq.17, we have introduced auxiliary functions $e_E(m)$ and $e_O(m)$, which satisfy^{††}:

$$e(m) \equiv \sum_{n \in \mathbb{Z}} \frac{q_n^2}{(p_m^2 + q_n^2)^2} = \frac{L_y^2}{2\pi} \left[\frac{-\pi}{\sinh^2(2\pi L_y m / L_x)} + \frac{L_x}{2m L_y} \frac{1}{\tanh(2\pi L_y m / L_x)} \right]$$

$$e_E(m) \equiv \sum_{n \in E} \frac{q_n^2}{(p_m^2 + q_n^2)^2} = 1/4 e(m/2)$$

$$e_O(m) \equiv \sum_{n \in O} \frac{q_n^2}{(p_m^2 + q_n^2)^2} = e(m) - 1/4 e(m/2)$$

Now, the infinite summation in Eq. 17 needs to be calculated. For a single plastic event located at (x_{ev}, y_{ev}) , that is, $\hat{\epsilon}^{pl}(m, n) = e^{-ip_m x_{ev}} e^{-ip_m y_{ev}} \left(\epsilon_{xx}^{pl}, \epsilon_{xy}^{pl} \right)^T$, the use of the expression for $\hat{u}_x^{*\infty}$ leads to:

$$\sum_{n' \in \delta} \hat{u}_x^{*\infty}(m, n') = 4e^{-ip_m x_{ev}} \left[\epsilon_{xy}^{pl} \left(p_m^2 \frac{L_y^3}{\pi^3} j_\delta(X) - \frac{L_y}{\pi} k_\delta(X) \right) - 2i \epsilon_{xx}^{pl} p_m \frac{L_y^2}{\pi^2} s_\delta(X) \right], \quad (18)$$

where the δ -subscript stands for either E or O , and $X \equiv (x, \alpha) \equiv \left(\frac{\pi y_{ev}}{L_y}, \frac{p_m L_y}{\pi} \right)$.

^{††} The analytical calculations leading to the second part of the equality involve the decomposition into simple elements and the use of well established summation results⁷⁷.

Inserting Eq.18 into Eq.17, summing the plastic activity of all lines y , i.e.^{‡‡}, $y = 0.5, \dots, L_y - 0.5$ ($L_y \in \mathbb{N}^*$) in the discretised version, and Fourier transforming the results along direction x via the operator \mathcal{F}_x , defined by $\mathcal{F}_x \sigma = 1/L_x \int \sigma(x) e^{-ipm^x} dx$, one finally arrives at :

$$\hat{u}^{corr}(m, n \in \delta) = \left(\begin{array}{cc} \overbrace{\left[\sum_y \left(\frac{P_m^2 L_y^2}{e_\delta(m) \pi^3} j_\delta(X) - \frac{1}{\pi} k_\delta(X) \right) \mathcal{F}_x \sigma_{xy}^{pl}(m, y) \right]}^{\equiv \zeta_\delta(X)} & -2i \sum_y \overbrace{\left(\frac{P_m L_y}{e_\delta(m) \pi^2} s_\delta(X) \right) \mathcal{F}_x \sigma_{xx}^{pl}(m, y)}^{\equiv \xi_\delta(X)} \\ \frac{4q_m^2}{4\mu q^4} \cdot \left[\sum_y \left(\frac{P_m^2 L_y^2}{e_\delta(m) \pi^3} j_\delta(X) - \frac{1}{\pi} k_\delta(X) \right) \mathcal{F}_x \sigma_{xy}^{pl}(m, y) \right] & -2i \sum_y \left(\frac{P_m L_y}{e_\delta(m) \pi^2} s_\delta(X) \right) \mathcal{F}_x \sigma_{xx}^{pl}(m, y) \\ \frac{4p_m q_m}{4\mu q^4} \left[\sum_y \left(\frac{P_m^2 L_y^2}{e_\delta(m) \pi^3} j_\delta(X) - \frac{1}{\pi} k_\delta(X) \right) \mathcal{F}_x \sigma_{xy}^{pl}(m, y) \right] & -2i \sum_y \left(\frac{P_m L_y}{e_\delta(m) \pi^2} s_\delta(X) \right) \mathcal{F}_x \sigma_{xx}^{pl}(m, y) \end{array} \right),$$

where new summations appear and can be expressed analytically via a decomposition into simple elements and the use of known summation formulae⁷⁷:

$$\begin{aligned} j(x, \alpha) &\equiv \sum_{k=-\infty}^{+\infty} \frac{k \sin(kx)}{(k^2 + \alpha^2)^2} = \frac{\pi}{2\alpha^2} \frac{\sinh(\alpha(\pi - x))}{\sinh(\alpha\pi)} - \frac{1}{2\alpha^2} \mathcal{H}(x, \alpha) \\ j_E(x, \alpha) &= 1/8 j(2x, \alpha/2) \\ \mathcal{H}(x \neq 0, \alpha) &\equiv \sum_{k=-\infty}^{+\infty} \frac{k \sin(kx)}{(k - i\alpha)^2} = \frac{h(x, \alpha) + h(x, -\alpha)}{2} \\ h(x \neq 0, \alpha) &\equiv -i \sum_{k=-\infty}^{+\infty} \frac{k \exp(ikx)}{(k - i\alpha)^2} = \frac{\pi \exp(-x\alpha)}{1 - \cosh(2\pi\alpha)} [x\alpha (e^{2\pi\alpha} - 1) + 2\pi\alpha - (e^{2\pi\alpha} - 1)] \\ k(x, \alpha) &\equiv \sum_{k=-\infty}^{+\infty} \frac{k^3 \sin(kx)}{(k^2 + \alpha^2)^2} = \frac{\pi \sinh(\alpha(\pi - x))}{2 \sinh(\alpha\pi)} + \frac{\mathcal{H}(x, \alpha)}{2} \\ k_E(x, \alpha) &= 1/2 k(2x, \alpha/2) \\ s(x, \alpha) &\equiv \sum_{k=-\infty}^{+\infty} \frac{k^2 \exp(ikx)}{(k^2 + \alpha^2)^2} = \frac{\pi \cosh(\alpha(\pi - x))}{2 \alpha \sinh(\alpha\pi)} + \frac{\pi}{4} u(x, \alpha) \\ s_E(x, \alpha) &= 1/4 s(2x, \alpha/2) \\ u(x, \alpha) &\equiv \frac{2x \cosh(\alpha(x - 2\pi)) + (2\pi - x) \cdot 2 \cosh(\alpha x)}{(1 - \cosh(2\pi\alpha))} \end{aligned}$$

The function j_O is obtained by writing $j(x, \alpha) = j_O(x, \alpha) + j_E(x, \alpha)$; the same applies for the other functions with subscripts O .

The coincidence of the infinite summations and their analytical expressions has been verified numerically for particular values of the parameters.

As a technical remark, we would like to mention that the preceding formulae are difficult to evaluate numerically for $|\alpha| \gg 1$, on account of the large arguments of the hyperbolic functions. Nevertheless, the following approximations provide very satisfactory results in the limit of large α 's ($\alpha > 0$) :

$$\frac{\sinh[\alpha(\pi - x)]}{\sinh(\alpha\pi)} \approx \exp(-x\alpha) - \exp(\alpha(x - 2\pi))$$

^{‡‡} The +0.5 term comes from the fact that the y -coordinate of a block (of unit size) is evaluated at its centre.

$$\frac{\cosh[\alpha(\pi - x)]}{\sinh(\alpha\pi)} \approx \exp(-x\alpha) + \exp(\alpha(x - 2\pi))$$

$$h(x, \alpha) \approx -2\pi \exp(-x\alpha) [x\alpha - 1]$$

$$u(x, \alpha) \approx -2[x \exp[\alpha(x - 4\pi)] + x \exp(-\alpha x) + (2\pi - x) \cdot \exp[\alpha(x - 2\pi)]]$$

Our final result is:

$$\begin{pmatrix} \sigma_{xx}^{corr}(m, n) \\ \sigma_{xy}^{corr}(m, n) \end{pmatrix} = \begin{pmatrix} \frac{-2\rho_m q_n^2}{q^4} \left[i \sum_y \zeta_\delta(X) \mathcal{F}_x \sigma_{xy}^{pl}(m, y) + 2 \sum_y \xi_\delta(X) \mathcal{F}_x \sigma_{xx}^{pl}(m, y) \right] \\ \frac{q_n (\rho_m^2 - q_n^2)}{q^4} \left[i \sum_y \zeta_\delta(X) \mathcal{F}_x \sigma_{xy}^{pl}(m, y) + 2 \sum_y \xi_\delta(X) \mathcal{F}_x \sigma_{xx}^{pl}(m, y) \right] \end{pmatrix}, \quad (19)$$

where we should note that $\zeta(0, n \in O) = \frac{-2}{L_y^2}$.

As a computational detail, note that the y -coordinates are here integers shifted by half unity, i.e., of the form $p + 1/2$, $p \in \mathbb{N}$, whereas computational routines for Fast Fourier Transform take as input an array with integer indices. It is therefore easier to suppose that the walls are at positions $y = -1/2$ and $y = L_y - 1/2$. This translation is readily achieved by simply multiplying the Fourier components of the correction term, as given above, by prefactors $\exp\left(\frac{iq_n}{2}\right)$.

Assuming a complexity $O(N \ln N)$ for the Fast Fourier Transform of an array of N cells, the number of operations performed at each time step of our algorithm is of order $O(L_x L_y^2 \ln L_x)$ for large integers L_y and L_x , as is evident from Eq.19.

B Calculation of the line-averaged velocity

The mean velocity on a line $y = y_0$ reads:

$$\begin{aligned} \langle u_x \rangle_x(y_0) &\equiv \frac{1}{L_x} \int_{-L_x/2}^{L_x/2} u_x(x, y_0) dx \\ &= \sum_{n=-\infty}^{+\infty} \hat{u}_x(m=0, n) e^{iq_n y_0} \\ &= \sum_{\substack{n=-\infty \\ n \neq 0}}^{+\infty} \hat{u}_x^{*\infty}(0, n) e^{iq_n y_0} + \hat{u}_x^{*\infty}(0, 0) - (1 - 2|y_0|/L_y) \sum_I \hat{u}_x^{*\infty}(0, \cdot) + \sum_P \overbrace{\hat{u}_x^{corr}(0, \cdot)}^0 e^{iq_n y_0} \\ &= \sum_{y_{ev}} \frac{a}{2\mu} \left[\text{Sign}(y_0 - y_{ev}) \cdot \left(1 - \frac{|y_0 - y_{ev}|}{L_y} \right) + 1 - \frac{y_{ev}}{L_y} - \frac{y_0}{L_y} \right] \mathcal{F}_x \sigma_{xy}^{pl}(m=0, y_{ev}), \end{aligned}$$

where the last summation is performed over all streamlines y_{ev} , and $\hat{u}_x^{*\infty}$ is the bulk contribution in the duplicated system.

C Estimation of the deviations due to bulk cooperativity

Assume the fluidity diffusion equation is a valid approximation,

$$\xi^2 \Delta f - (f - f_{bulk}) = 0$$

where $f = \frac{\dot{\gamma}}{\sigma}$ is the local fluidity, and ξ is a cooperativity length that may vary with the shear rate.

Let $\delta f = f - f_{bulk}$ be the deviation from the expected fluidity profile owing to cooperative effects between regions subject to different driving forces.

One now assumes $\delta f \ll f_{bulk}$ and $\Delta \delta f \ll \Delta f_{bulk}$.

To leading order, the fluidity diffusion equation reads

$$\xi^2 \Delta f_{bulk} = \delta f$$

The amplitude of the deviations due to cooperativity is given by the Babel number

$$\text{Ba} \equiv \frac{\delta f}{f} \approx \xi^2 \frac{\Delta f_{bulk}}{f_{bulk}}$$

If the flow curve follows a Herschel-Bulkley law: $\sigma(\dot{\gamma}) = \sigma_d + A\dot{\gamma}^n$,

$$f'_{bulk} = \frac{\sigma^2}{A^{1/n}} \frac{\sigma^{n-1} (\sigma - \sigma_d)^{1/n-1}}{n} \left[\left(\frac{1}{n} - 1 \right) \frac{\sigma^{-n}}{\sigma - \sigma_d} \left((1-n) + n \frac{\sigma_d}{\sigma} \right)^2 - n \sigma^{-n-1} \left(1 - n + (1+n) \frac{\sigma_d}{\sigma} \right) \right]$$

Here, the primes denote derivatives with respect to the space coordinate. Then,

$$\frac{f''_{bulk}}{f_{bulk}} = \frac{\sigma^2}{n(\sigma - \sigma_d)} \left[\frac{(1/n - 1)}{\sigma - \sigma_d} \left((1-n) + n \frac{\sigma_d}{\sigma} \right)^2 - \frac{n}{\sigma} \left(1 - n + (1+n) \frac{\sigma_d}{\sigma} \right) \right]$$

To leading order, one finally arrives at $\frac{\delta f}{f} \sim \xi^2 \frac{\sigma^2}{(\sigma - \sigma_d)^2}$.